A new hybrid lattice-Boltzmann method for thermal flow simulations in low-Mach number approximation

Guanxiong Wang, Song Zhao, Pierre Boivin, Eric Serre, Pierre Sagaut

A new hybrid Lattice-Boltzmann method for thermal flow simulations in low-Mach number approximation

Guanxiong WANG (王冠雄),[1] Song ZHAO (赵崧),[1] Pierre BOIVIN,[1] Eric SERRE,[1] and Pierre SAGAUT[1]

Aix-Marseille Univ., CNRS, Centrale Marseille, M2P2, Marseille, France

(*Electronic mail: guanxiong.wang.isae@hotmail.com)

(Dated: 11 April 2022)

A new low-Mach algorithm for the thermal Lattice Boltzmann method (LBM) is proposed aiming at reducing the computational cost of thermal flow simulations in the low Mach number limit. The well known Low Mach Number Approximation (LMNA) is adopted to accelerate the simulations by enlarging the time-step through re-scaling the pseudo acoustic speed to the same order of the fluid motion velocity. This specific process is inspired by the similarity between the artificial compressibility method and the isothermal LBM, and is further extended to its thermal counterpart. It must be emphasized that such low-Mach acceleration strategy is in a general form, thus can be easily applied to other compressible LB methods. The present method overcomes the drawback of classical PGS (Pressure Gradient Scaling) method due to the pressure gradient changing. The new algorithm is validated by various well-documented academic test cases in laminar (1D (one dimensional) gravity column, 2D (two dimensional) rising thermal bubble, 2D differentially heated square cavity) and turbulent (3D (three dimensional) Taylor-Green vortex and 3D heated cylinder) regimes. All the results show excellent agreement with the reference data and high computational efficiency.

I. INTRODUCTION

Low-speed thermal flows (low-Mach number limit) have been of scientific interest for a long time due to their fundamental importance in the study of buoyancy driven thermal flows and their relevance with many technological and geophysical processes. Cooling systems for automobiles and nuclear reactors, as well as heat exchangers for turbomachinery and electronic devices, are examples of typical engineering applications. Flow simulations based on the Boussinesq approximation (BO) have proliferated in the literature since the seminal work of Gordon Draisey *et al.*[1]. However the BO approximation is only valid for small temperature differences[2] (i.e., $\Delta T/T_0 < 0.1$) and all thermal properties such as the expansion coefficient, viscosity and heat conductivity are held constant. Nevertheless, in many applications, non-Boussinesq conditions with variable thermodynamic properties prevail due to large density or temperature differences[3]. In this circumstance, the fully compressible Navier-Stokes system must to be considered. However the system's inherent fast acoustic waves are expensive to model numerically and moreover irrelevant in most convection flows at low speed. When compared to implicit schemes, explicit time discretization requires a smaller time step to meet the Courant-Friedrich-Lewy (CFL) stability condition, while implicit systems may have convergence issues due to poor conditioning of the convective fluxes of Jacobian matrix. Furthermore, the solution of the discrete equations contains pressure fluctuations of the order of the Mach number Ma, whereas the continuous equations only have pressure fluctuations on the order of Ma^2, resulting in a loss of accuracy[4] Therefore, low Mach thermal flow simulations remain challenging despite ongoing development due to the issue of finding the appropriate trade-off between algorithm accuracy and numerical efficiency.

One common and simple strategy to improve the computational efficiency is the Pressure Gradient Scaling (PGS) method[5] with an acceleration coefficient $\alpha_{\mathrm{PGS}} > 1$. This method artificially reduces the effective speed of sound by a factor α_{PGS}, which automatically increases the time step by nearly the same factor. However, the PGS method has an inherent disadvantage that stems from the modification of one dominant term in the governing equation, which can be a serious issue, particularly when the flow dynamics are controlled by external forces such as buoyancy[6]. This is not the case of another well-suited approach for dealing with heat dominated flows at arbitrary large density differences - the so-called low Mach number approximation (LMNA). This approximation filters the acoustic waves from the Navier-Stokes equations using an asymptotic expansion in powers of the Mach number. In practice, at least two scaling methods are possible depending on the temperature variation[7–9], while the truncating order $O(Ma^2)$ is widely considered and adopted in this investigation[4,10]. The pressure $p(x,t)$ is then splitted into a thermodynamic pressure $p(t)$, which varies with time but is spatially homogeneous, and a hydrodynamic pressure $p^h(x,t)$, i.e., $p(x,t) = p(t) + O(Ma^2)p^h(x,t)$. The total pressure is substituted by the thermodynamic pressure $p(t)$, except in the momentum equation, which decouples the pressure and density fluctuations and filters the sound waves from the system. Particularly, only thermodynamic pressure is taken into account in the law of state. The velocity field is no longer divergence free, and the spatial and temporal variations of density introduce additional nonlinearities into the equations. Nonetheless, similar numerical approaches can still be employed because these equations have the same mixed hyperbolic-parabolic character as the equations for incompressible flow. The low Mach equations have already been applied successfully to research on natural convection, combustion, astrophysical flows and others (see some relevant examples in Bouloumou *et al.*[11]).

In this study, we try to include the LMNA strategy into the Lattice Boltzmann method (LBM) and use this approach to simulate low-Mach number thermal flows. The decision to choose LBM is straightforward because of its attractive inherent properties such as simplicity to implement and parallelize, which provides a high computational efficiency for unsteady complex flows[12,13]. Originally designed for weakly compressible isothermal approaches, many attempts have been conducted to extend LBM capabilities to deal with more complex configurations such as high subsonic and supersonic flow dynamics[14–19], compressible thermal problems[20–22], turbulent flows[23], reactive flows[24,25] and others. For small temperature differences, thermal effects can be included using the BO approximation (see for example in litteratures[26–28]) which corresponds to a decoupling model and resolves an incompressible system with a linearized buoyancy force. In other configurations (corresponding to the fully compressible Navier-Stokes system), thermal effects are included either using another distribution function (Double Distribution Function - DDF approach) or either by solving an energy equation (hybrid approach) with a perfect gas law[21,29]. Most of these approaches investigate laminar flows and have been rarely extended to turbulent complex flows in low-Mach number limit.

Being intrinsically based on explicit time marching schemes, LBM's time-stepping is constrained by the Courant-Friedrich-Lewy (CFL) number (i.e., $\mathrm{CFL}_{\mathrm{ac}} \equiv \max\left[\frac{(|\boldsymbol{u}|+c)\Delta t}{\Delta x}\right] \leq \mathrm{CFL}_{\mathrm{max}}$). Thus, when using a compressible model to simulate a low-Mach number flow, the time-step is strongly constrained by the fast acoustic waves scale, which strongly penalizes the numerical efficiency of the solver[30]. To overcome this issue, several LB algorithms have been developed in the

LMNA, by modifying classical isothermal LB algorithm, i.e., zeroth-order moment of the hydrodynamic pressure[31–36]. In such algorithms, additional terms need to be added to correctly recover Navier-Stokes equations in LMNA, thus making the resolved system complicated to understand and difficult to extend to other applications.

This paper proposes a new algorithm for the hybrid LBM in the LMNA for simulating low-Mach number thermal flows. This low-Mach number algorithm only involves minor changes in the compressible LBM that makes it easy to implement and nearly independent of the thermal LBM used. The present method is evaluated on well-documented test cases of the literature for both simple laminar thermal flows and complex turbulent heat transfer problems. The 1D gravity column and the 2D rising bubble are considered to show the superiority of the new algorithm on the Pressure Gradient scaling commonly used to improve the computational efficiency of LBM. Then, a classical 2D non-Boussinesq natural convection flow is considered in a differentially heated square cavity at Rayleigh number 10^7. The 3D Taylor-Green vortex flow at Reynolds number $Re = 1.2 \times 10^4$ is chosen to assess the ability of the present method to evaluate viscous tensor. The final test case is the flow around a 3D heated cylinder at $Re = 3900$, to evaluate the performance of the present method to predict complex thermal turbulent flow.

The rest of the paper is organized as follows: §II introduces the general low-Mach number acceleration strategy adopted in this study and details the incorporation of low-Mach approach within the hybrid compressible LBM framework. Then, in §III the code is benchmarked with respect to numerical data from the literature for five test cases. At last, a conclusion with a summary of the speedup is drawn in §IV.

II. THE HYBRID LBM SOLVER IN THE LOW-MACH NUMBER APPROXIMATION

As mentioned in the introduction, the low-Mach number approximation (LMNA) of the Navier-Stokes equations is a very popular and efficient way to simulate low-Mach number flows at a macroscopic level (Appendix A). However, it involves a Poisson equation to resolve the hydrodynamic pressure p^h which makes it not directly applicable in the LBM framework while keeping the locality feature.

We consider here the hybrid LBM for solving compressible flows and its extension to the low-Mach number approximation proposed in this paper.

A. The hybrid LBM solver for compressible flows

A complete description of the hybrid LBM is provided in literature.[18,37,38]. In this method, the mass and momentum equations are solved using LBM, while the entropy equation is resolved using Finite Difference method (FDM). Three major steps detailed below are needed to obtain the variables at time step $t+\Delta t$ from the variables at t: a *local* collision step, a *linear* streaming step and the updating of macroscopic variables.[1]

Thus, the three steps of the algorithm write as:

- **Step I: Collision.** The collision distribution function is calculated as

$$f_i^{\mathrm{col}}(\boldsymbol{x},t) \equiv f_i^{\mathrm{eq}}(\boldsymbol{x},t) + \left(1-\frac{\Delta t}{\tau}\right) f_i^{\mathrm{neq}}(\boldsymbol{x},t) + \frac{\Delta t}{2} F_i(\boldsymbol{x},t)\ , \tag{1}$$

  where

  I.1 The equilibrium distribution f_i^{eq} is constructed in a regularized manner on the basis of the lattice, i.e.

$$f_i^{\mathrm{eq}} = \omega_i \left\{ a^{(0),\mathrm{eq}} + \frac{\mathscr{H}^{(1)}_{i,\alpha}}{c_s^2} a^{(1),\mathrm{eq}}_{\alpha} + \frac{\mathscr{H}^{(2)}_{i,\alpha\beta}}{2c_s^4} a^{(2),\mathrm{eq}}_{\alpha\beta} + \frac{\mathscr{H}^{(3)}_{i,\alpha\beta\gamma}}{6c_s^6} a^{(3),\mathrm{eq}}_{\alpha\beta\gamma} + \frac{\mathscr{H}^{(4)}_{i,\alpha\beta\gamma\delta}}{24c_s^8} a^{(4),\mathrm{eq}}_{\alpha\beta\gamma\delta} \right\}\ , \tag{2}$$

  where ω_i is the weight for direction i, c_s the lattice sound speed ($\Delta x/(\sqrt{3}\Delta t)$ in D3Q19 lattice), $\mathscr{H}$ the Hermite polynomial basis with α, β,γ,δ being the coordinate indices. They are all constants only depending on the lattice applied. a^{eq} are the coefficients of the equilibrium distribution projected on the basis $\mathscr{H}$. They can be different from one LBM kernel to another, but in any case, they only depend on local density ρ, velocity $\mathbf{u}$, and a normalized temperature $\theta \equiv \frac{p}{\rho c_s^2}$ where p represent the pressure. Detailed expressions of the basis as well as the coefficients can be found in Farag *et al*.[18,37].

  I.2 The off-equilibrium distribution f_i^{neq} is evaluated on second and third order basis as

$$f_i^{\mathrm{neq}} = \omega_i \left[\frac{\mathscr{H}^{(2)}_{i,\alpha\beta}}{2c_s^4} a^{(2),\mathrm{neq}}_{\alpha\beta} + \frac{\mathscr{H}^{(3)}_{i,\alpha\beta\gamma}}{6c_s^6} a^{(3),\mathrm{neq}}_{\alpha\beta\gamma} \right]\ . \tag{3}$$

  where the coefficients of the non-equilibrium population on the basis $a^{(2),\mathrm{neq}}_{\alpha\beta}$ and $a^{(3),\mathrm{neq}}_{\alpha\beta\gamma}$ is evaluated through a hybrid recursive procedure introduced by Jacob *et al*.[23].

[1] The equations in the algorithm are normalized by LBM units, i.e. $x_\infty \equiv \Delta x$, $t_\infty \equiv \Delta t$.

I.3 The forcing term F_i is added to recover correct effects of viscous and external force (e.g. gravity),

$$F_i \equiv F_i^E + F_i^g \ , \tag{4}$$

in which the force F_i^E correct the higher order defects of the lattice to maintain the required stress tensor as in Eq. (A3c). Its exact expression can be found in[18,37,38]. The gravity is considered through

$$F_i^g = \omega_i \left[\frac{\mathscr{H}_{i,\alpha}^{(1)}}{c_s^2} \rho g_\alpha + \frac{\mathscr{H}_{i,\alpha\beta}^{(2)}}{2c_s^4} (\rho u_\alpha g_\beta + \rho u_\beta g_\alpha) \right] \ . \tag{5}$$

- **Step II: Streaming.** The collision distribution is streamed to its corresponding neighbor, i.e.

$$f_i(\boldsymbol{x}, t+\Delta t) = f_i^{\mathrm{col}}(\boldsymbol{x} - \boldsymbol{c_i}\Delta t, t) \tag{6}$$

where $\boldsymbol{c_i}$ is the vector pointing from the current node to its i^{th} neighbor.

- **Step III: Macroscopic variable update.**

III.1 The entropy equation is discretized using a explicit Euler time stepping, together with the flux and viscous terms calculated with FDM.

III.2 The density and momentum fields are updated using the distributions

$$\rho(\boldsymbol{x}, t+\Delta t) = \rho(\boldsymbol{x}, t) + \sum_i \left[f_i(\boldsymbol{x}, t+\Delta t) - f_i^{\mathrm{col}}(\boldsymbol{x}, t) \right] \tag{7a}$$

$$\rho u_\alpha(\boldsymbol{x}, t+\Delta t) = \sum_i c_{i\alpha} f_i(\boldsymbol{x}, t+\Delta t) + \frac{\Delta t}{2} \rho(\boldsymbol{x}, t+\Delta t) g_\alpha \tag{7b}$$

We propose now to adapt this hybrid LBM solver in the low-Mach number approximation.

B. The hybrid LBM solver in the low-Mach number approximation

The LMNA is adapted here to the compressible LBM by analyzing the classical iso-thermal LBM. In fact, in athermal LBM, the "pressure" is nothing but a scaled density such as

$$p^{\mathrm{LBM}} \equiv \rho c_s^2 \tag{8}$$

It is updated at each time step by

$$
\begin{aligned}
p^{\mathrm{LBM}}(\boldsymbol{x},t+\Delta t) &\equiv c_s^2 \rho(\boldsymbol{x},t+\Delta t) \\
&= c_s^2 \left\{ \rho(\boldsymbol{x},t) + \sum_{i=1}^{Q} \left[f_i^{\mathrm{col}}(\boldsymbol{x}-\boldsymbol{c_i}\Delta t,t) - f_i^{\mathrm{col}}(\boldsymbol{x},t) \right] \right\} \\
&\approx p^{\mathrm{LBM}}(\boldsymbol{x},t) - \Delta t c_s^2 \frac{\partial \rho u_\alpha}{\partial x_\alpha}(\boldsymbol{x},t) \\
&= p^{\mathrm{LBM}}(\boldsymbol{x},t) - \Delta t \frac{\partial p^{\mathrm{LBM}} u_\alpha}{\partial x_\alpha}(\boldsymbol{x},t) \\
&= p^{\mathrm{LBM}}(\boldsymbol{x},t) - \Delta t \left\{ u_\alpha \frac{\partial p^{\mathrm{LBM}}}{\partial x_\alpha}(\boldsymbol{x},t) - \rho c_s^2 \frac{\partial u_\alpha}{\partial x_\alpha} \right\}
\end{aligned} \tag{9}
$$

As pointed out by He *et al.*[39], under low-Mach assumption, this equation mimics the acoustic pressure transport except that the physical speed of sound c in the last term is substituted by the lattice sound speed c_s. This makes the isothermal LBM an artificial compressibility method[40] where the transport of acoustic pressure fields are modified to adapt the permitted time step of the numerical schemes[39].

We now extend the same idea to thermal LBM. Unfortunately, the temperature/density gradients in low-Mach thermal flow fields can be relatively large, such that the flow dilatation $\partial(\rho u_\alpha)/\partial x_\alpha$ might break the scale balance in equation (9). At this stage, we just remove its "thermal" part ($-\partial\rho/\partial t$), and only apply its "hydrodynamic" part for the hydrodynamic pressure transport, i.e.

$$
\begin{aligned}
p^h(\boldsymbol{x},t+\Delta t) &= p^h(\boldsymbol{x},t) + c_s^2 \left\{ \sum_{i=1}^{Q} \left[f_i^{\mathrm{col}}(\boldsymbol{x}-\boldsymbol{c_i}\Delta t,t) - f_i^{\mathrm{col}}(\boldsymbol{x},t) \right] - \left[\rho(\boldsymbol{x},t+\Delta t) - \rho(\boldsymbol{x},t) \right] \right\} \\
&\approx p^h(\boldsymbol{x},t) - \Delta t c_s^2 \frac{\partial (\rho u_\alpha)^h}{\partial x_\alpha} \\
&\approx p^h(\boldsymbol{x},t) - \Delta t \left[u_\alpha \frac{\partial \rho^h c_s^2}{\partial x_\alpha} + \rho^h c_s^2 \frac{\partial u_\alpha}{\partial x_\alpha} + u_\alpha^h \frac{\partial \rho c_s^2}{\partial x_\alpha} + \rho c_s^2 \frac{\partial u_\alpha^h}{\partial x_\alpha} \right]
\end{aligned} \tag{10}
$$

Compared to the theoretical transport equation of the hydrodynamic pressure, one can find again that the speed of sound is substituted by c_s. Similar to the athermal LBM, the CFL constrain of such system is now related to c_s instead of c. In practice, we still want to conserve the low-Mach property, i.e.,

$$
c_s \equiv \frac{\Delta x}{\sqrt{3}\Delta t} \geq 3|\boldsymbol{u}|_{\max} . \tag{11}
$$

Now the time step is constrained by the flow speed instead of the speed of sound. In low-Mach number applications, this will give us a much larger Δt that will accelerate the calculation. Similar to every other LMNA method, this approach only modifies small scale quantities under low-Mach conditions, so that it will not suffer from the problem of PGS method when external forces are under consideration.

Such strategy can be easily applied to any compressible LBM. The following algorithm shows how all variables are advanced from time step t to $t+\Delta t$

- **Step I: Collision.** It remains the same as for the compressible LBM, except that the reduced "temperature" for the low-Mach version is now defined as

$$\theta \equiv \frac{p^h}{\rho c_s^2} \; . \tag{12}$$

- **Step II: Streaming.** It remains the same as the compressible LBM.

- **Step III: Macroscopic variable updating.**

III.1 The entropy equation (A3d) is resolved in the same manner as in the compressible LBM.

III.2 The thermodynamic pressure $p(t+\Delta t)$. In open systems, it can be set directly to the ambient pressure. For closed configurations, it can be evaluated through global mass conservation, see appendix B.

The density field is evaluated through the equation of state (EOS) (A3e), i.e.

$$\rho(\boldsymbol{x},t+\Delta t) = \left[\frac{p(t+\Delta t)}{\mathrm{e}^{s(\boldsymbol{x},t+\Delta t)/c_v}}\right]^{1/\gamma} \tag{13}$$

The momentum fields are updated the same as in compressible solver.

The hydrodynamic pressure field is updated using equation (9), i.e.

$$p^h(\boldsymbol{x},t+\Delta t) = p^h(\boldsymbol{x},t) + c_s^2 \left\{ \sum_i \left[f_i(\boldsymbol{x},t+\Delta t) - f_i^{\mathrm{col}}(\boldsymbol{x},t) \right] - \left[\rho(\boldsymbol{x},t+\Delta t) - \rho(\boldsymbol{x},t)\right] \right\} \tag{14}$$

This low-Mach algorithm involves three changes with respect on the compressible LBM of §II A:

- i) The hydrodynamic pressure is used instead of the pressure field equilibrium population evaluation.

- ii)The density is solved through EOS instead of using LBM populations.
- iii) The hydrodynamic pressure is transported in step III.

This means that it is almost independent of the original thermal LBM scheme. In practice, it will be successfully applied in this paper to the pressure-based, the modified density-based and the unified LBM framework[18,37]. This is a major benefit of the current implementation compared to other low-Mach LBM approaches based on iso-thermal LBM[34,35]. It also permits us to keep some ingredients of the original LBM without any modification. For instance, the turbulence and wall models[22,41] keep working out in this low-Mach version.

III. VALIDATION TESTS

The proposed low-Mach thermal Lattice Boltzmann solver is now assessed by a variety of test cases related to low-Mach thermal flows. In order to show the efficiency of the present solver (LMNA), numerical results are compared to simulations obtained using a fully compressible solver, i.e., the classical Hybrid Recursive Regularization pressure-based HRR-p solver[18,37], and using the PGS method[5] (The PGS method is realized by multiplying pressure by a factor $1/\alpha_{PGS}^2$). The following validation tests are investigated:

- One-dimensional gravity column and 2D rising thermal bubble for which the fluid dynamics is dominated by pressure gradient and external force, i.e., buoyancy.
- 2D natural convection in a closed square cavity at Rayleigh number $\mathrm{Ra} = 10^7$.
- 3D Taylor Green Vortex flow at $Re = 1.2 \times 10^4$.
- 3D turbulent flow around a heated cylinder at $Re = 3900$.

A. One-dimensional gravity column

The one-dimensional gravity column is firstly considered to evaluate the ability of LMNA on capturing the balance between hydrodynamic pressure gradient with external force. The configuration consists of a 1D vertical column filled by air with pressure uniformly distributed. The gravity drives the fluid motion in the beginning till a converged static state is attained with a constant pressure gradient $\nabla p = \rho_0 g$.

In order to emphasize the computational efficiency of LMNA, simulations are also performed using PGS method and the fully compressible (HRR-p) solver. For the latter, the time step is fixed at $\Delta t = 1.65 \times 10^{-4} s$, whereas LMNA and PGS allow to consider a time step ten times larger equal to $\Delta t = 1.65 \times 10^{-3}$ that speeds up the computations of the same factor.

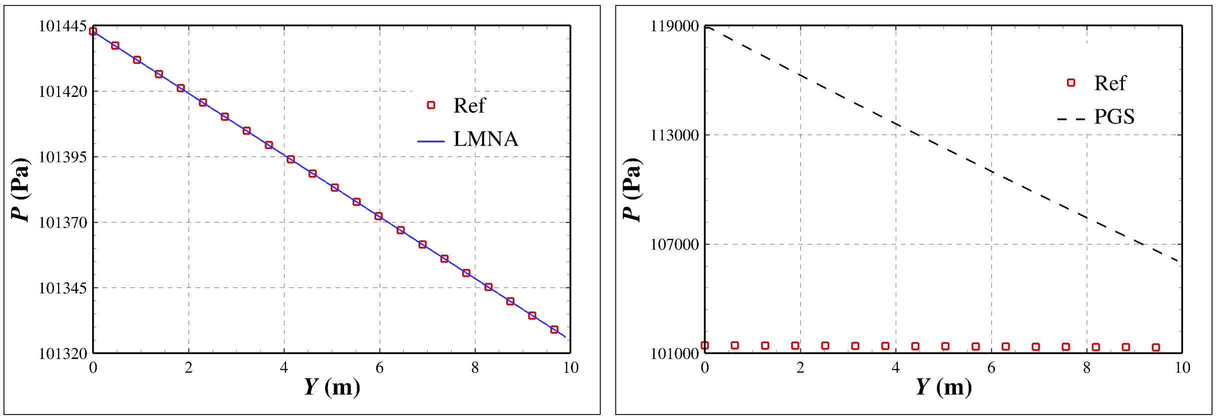

(a) (b)

FIG. 1. Comparison of the pressure profiles obtained from LMNA (a) and PGS (b) simulations and with the fully compressible (HRR-p) solver which is considered as the reference.

Fig. 1 shows the pressure profiles obtained from LMNA, PGS and the fully compressible (HRR-p) solver simulations, the latter being considered as the reference solution. The LMNA result matches perfectly the reference profile, while the PGS result amplifies by a factor of about 100 compared to the reference profile due to the re-scaled parameter $\alpha_{PGS} = 10$.

B. 2D rising thermal bubble

The rising thermal bubble configuration is dominated by gravity and pressure with thermal effect. The numerical configuration consists of a hot thermal bubble with a core temperature equal to 1200K that emerges in an atmosphere temperature of 300K. The width and height of the computational domain is respectively 20m and 15m. The bottom surface is configured to be a non-slip adiabatic wall, while the side and top boundaries are set to outlets with given pressure.

The maximum time step adopted by the fully compressible solver is equal to $\Delta t = 5.77 \times 10^{-5} s$, whereas LMNA and PGS allow to consider a time step around 25 times larger equal to $\Delta t = 1.44 \times 10^{-3}$ that speeds up the computations of the same factor. Buoyancy with a gravity $g = 9.81 \mathrm{m\,s^{-2}}$ drives the fluid motion, the bubble rises and deforms during the rising process.

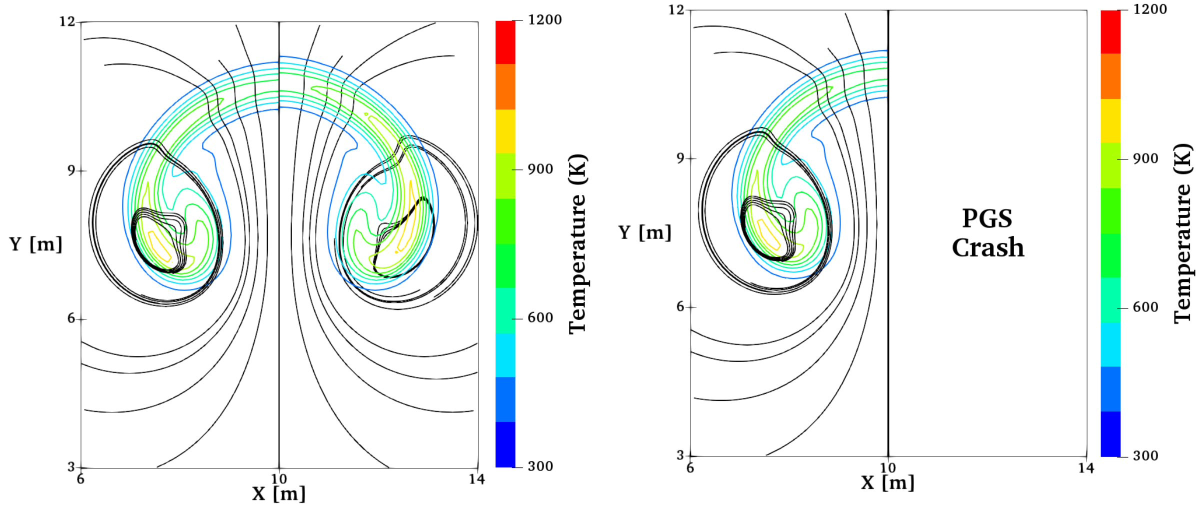

(a) (b)

FIG. 2. Comparisons of 2D temperature contours together with streamlines showing the rising bubble. For each plot, the left hand side corresponds to the fully compressible (HRR-p) solver simulation considered as the reference. (a) on the right hand side, LMNA simulation. (b) on the right hand side, PGS simulation which is crashed.

The temperature contours and streamlines are shown on Fig. 2. The LMNA simulation provides a result very similar to the reference solution with only negligible differences. However, the PGS simulation crashes using the same time step as LMNA. These results are consistent with the drawback of PGS as pressure plays a dominant role balancing the external force and viscous effects during the thermal bubble rising process. Consequently, the change of pressure gradient in PGS method leads to either incorrect results, i.e., one-dimensional gravity column in §III A or simulation crash as in this test case. By contrast, LMNA is able to provide the same results as with the fully compressible (HRR-p) solver, but with a time step between 10 and 25 times larger that allows much more efficient computations in these two low-Mach number configurations.

C. 2D natural convection inside a square cavity

This validation test has been intensively investigated in the literature both experimentally and numerically[42–47]. Many benchmarks exist and solutions are available in the literature[46,47]. The canonical configuration consists of a square cavity with two vertical differentially heated walls, and two horizontal adiabatic ones ($\frac{\partial T}{\partial n} = 0$) as shown in Fig. 3. The fluid motion is driven by the buoyancy force ($g = 9.81\mathrm{m\,s^{-2}}$), i.e., the fluid floats nearby the heat side wall whereas it sinks close to cold side wall thus generating a vortex inside the cavity. In this case, a large temperature

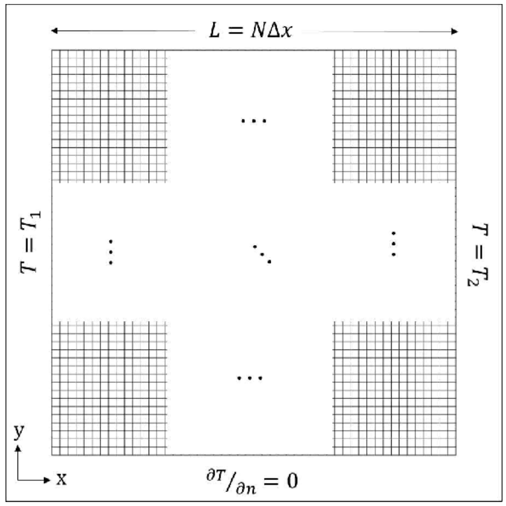

FIG. 3. Sketch of the 2D differentially heated square cavity together with boundary conditions and a Cartesian mesh.

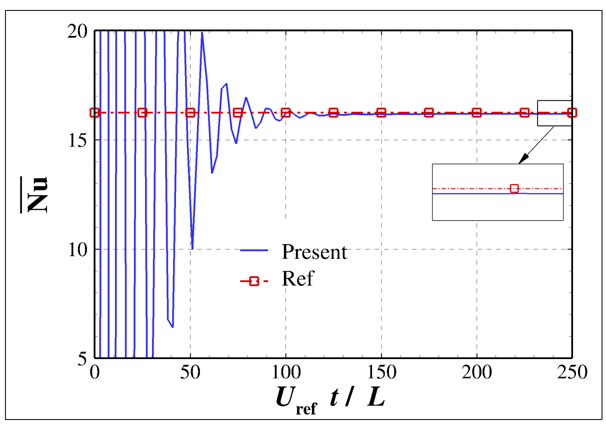

FIG. 4. Convergence in time of the average Nusselt number at Ra = 10^7. Present LMNA result ($Nu = 16.19$) and benchmark solution ($Nu = 16.24$)[47] as reference.

difference is considered to be beyond the Boussinesq validity limit, with the two vertical walls heated respectively at $T_1 = 240$K and $T_2 = 960$ K. This corresponds to a normalized temperature difference equal to $\varepsilon = \frac{T_1 - T_2}{T_1 + T_2} = 0.6$, which is indeed far beyond the Boussinesq validity limit $\varepsilon < 0.1$[44,45]. The fluid considered is air, and the dynamic viscosity is computed using the Sutherland's law $\mu(T) = \mu_0 (\frac{T}{T^*})^{3/2} \frac{T^* + S}{T + S}$ with $T^* = 273$K, $S = 110.5$K, $\mu_0 = 1.68 \times 10^{-5}$ kg m^{-1}s^{-2}. Then the thermal conductivity is calculated by $\lambda(T) = \frac{\mu(T)C_p}{Pr}$, where C_p being the specific heat capacity of air, and Pr being the Prandtl number equal to 0.71.

The thermal physics is characterized by a dimensionless number:

$$Ra = \frac{g\rho_0^2 \Delta T L^3 Pr}{T_0 \mu_0^2} \tag{15}$$

where ρ_0, μ_0 is the density and dynamic viscosity at mean temperature $T_0 = \frac{T_1+T_2}{2} = 600\text{K}$. The Rayleigh number $Ra = 10^7$ is chosen as it's related to the strongest heat convection effects over the range $10^3 - 10^7$ which is widely investigated[46,47].

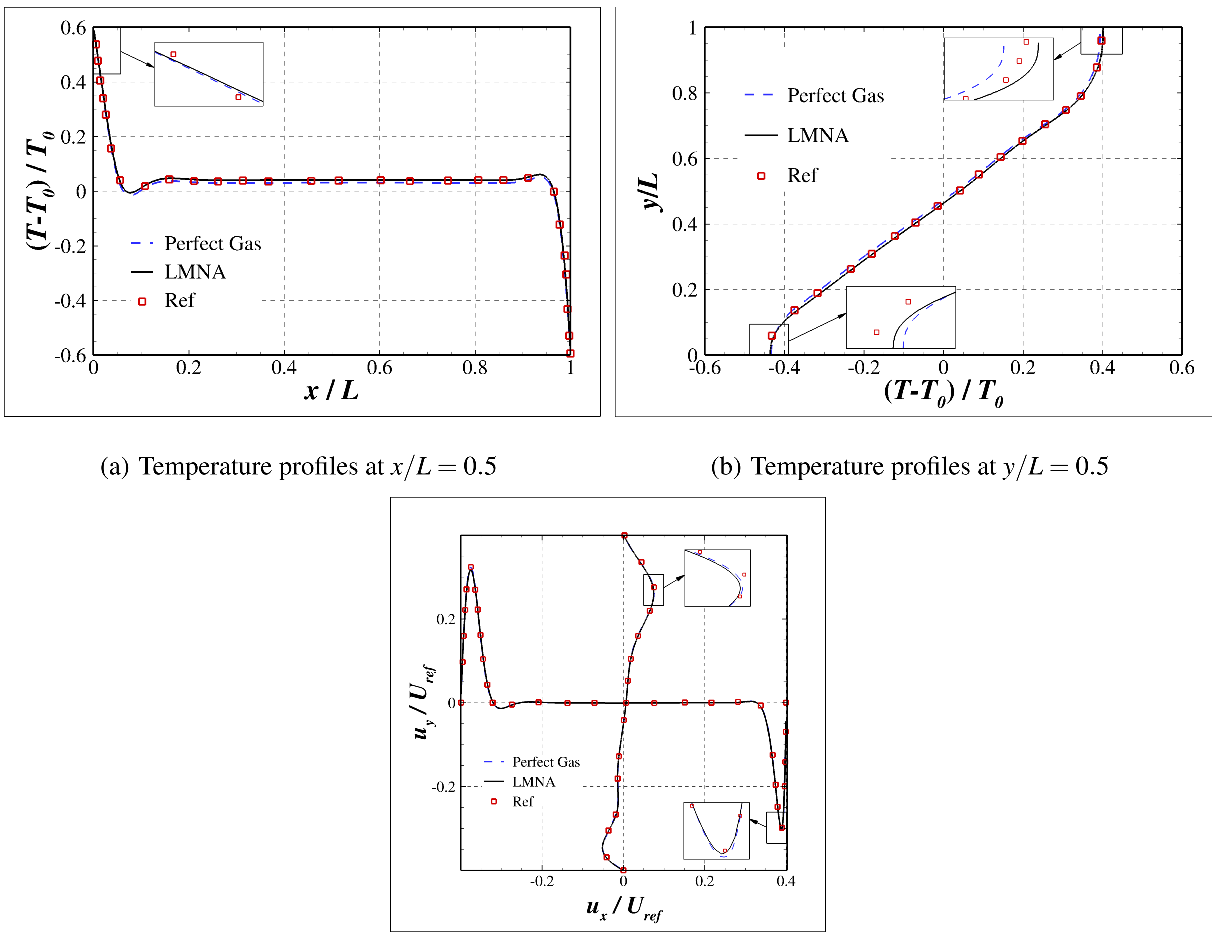

(a) Temperature profiles at $x/L = 0.5$

(b) Temperature profiles at $y/L = 0.5$

(c) Velocity profiles

FIG. 5. Profiles of temperature ((a)-(b)) and velocity (c) at Rayleigh number $Ra = 10^7$. Comparison between the present LMNA result (solid line), the fully compressible (HRR-p) result (dashed lines), and the benchmark solution[47] (markers).

The grid resolution is $N = \frac{L}{\Delta x} = 400$ in both directions, as proposed by Wang *et al.*[22]. The time steps adopted in the present LMNA and the fully compressible solver (HRR-p) are respectively equal to $\Delta t = 2.32 \times 10^{-5}$s and $\Delta t = 4.17 \times 10^{-7}$s. There is thus a factor of about 55.6 in the time steps of the two simulations showing again the superior efficiency of the LMNA in this type of low-Mach number flow configuration.

The heat flux at the heated wall is estimated by the Nusselt number and by its average over the heated wall, defined as follows:

$$Nu(y) = \frac{L}{\lambda_0 \Delta T} \lambda \frac{\partial T}{\partial x} \mid_{wall} \qquad \overline{Nu} = \frac{1}{L} \int_{y=0}^{y=L} Nu(y) dy \tag{16}$$

Time evolution of the average Nusselt number is plotted in Fig. 4, over a total dimensionless time $U_{ref} t/L = 250$, long enough to ensure the convergence as proposed by Wang *et al*.[22], where $U_{ref} = \frac{Ra^{0.5} \mu(T_0)}{\rho_0 L} \approx 1.1 \mathrm{m\,s^{-1}}$ is the reference velocity at $Ra = 10^7$. As shown in Fig. 4, the average Nusselt number provided by the LMNA simulation ($Nu = 16.19$)converges to the value of the benchmark solution ($Nu = 16.24$)[47] that corresponds to a difference less than 0.3%.

The flow features including the temperature distribution and velocity profiles are displayed in Fig. 5. The boundary layer close to the heated wall is well captured by LMNA as shown in Fig. 5(c). The high heat flux due to high temperature variations in the thermal boundary layer (see Fig. 5(b)) is also correctly predicted compared to the benchmark solution[47] and the one obtained with the fully compressible (HRR-p) solver[22].

D. Taylor Green Vortex

The investigation of Taylor Green Vortex (TGV) is aimed at assessing the ability of the present LMNA method of predicting the viscous tensor. The results and the computational efficiency of the classical pressure-based method reported by Tayyab *et al*.[25] are included as a reference. Pure fluid component (air) is considered and the Reynolds number investigated in this study is $Re = 1.2 \times 10^4$.

The flow field and hydrodynamic pressure field are initialized using an analytic N-S and Poisson solution respectively given by:

$$u_x(x,y,z) = u_0 \sin\left(\frac{2\pi x}{L}\right) \cos\left(\frac{2\pi y}{L}\right) \cos\left(\frac{2\pi z}{L}\right) \tag{17a}$$

$$u_y(x,y,z) = u_0 \cos\left(\frac{2\pi x}{L}\right) \sin\left(\frac{2\pi y}{L}\right) \cos\left(\frac{2\pi z}{L}\right) \tag{17b}$$

$$u_z(x,y,z) = 0 \tag{17c}$$

$$p^h(x,y,z) = \frac{1}{16} \rho_0 u_0^2 \left[\cos\left(\frac{4\pi x}{L}\right) + \sin\left(\frac{4\pi y}{L}\right)\right] \left[2 + \cos\left(\frac{4\pi z}{L}\right)\right] \tag{17d}$$

The initial velocity is $u_0 = 1\mathrm{m\,s^{-1}}$, and the viscosity is set to $\mu = 0.625\times10^{-3}\mathrm{kg\,m^{-1}\,s^{-1}}$. The thermodynamic pressure is the atmospheric pressure, i.e., $P_0 = 101325.0$ Pa, and the temperature is at $T = 300$K. Thus, density is taken as $\rho = P_0/(rT) = 1.172$ kg m^{-3} where $r = 287.15\mathrm{m^2\,s^{-2}\,K^{-1}}$ is the specific gas constant. The fluid domain is periodic with for each side $L = 2\pi$ m. The time step allowed by LMNA is $\Delta t = 1.89\times10^{-3}$s, compared to $\Delta t = 2.69\times10^{-5}$s used by the classical pressure-based method reported by Tayyab *et al*.[25]. This leads to a speed up of 70 in the computation.

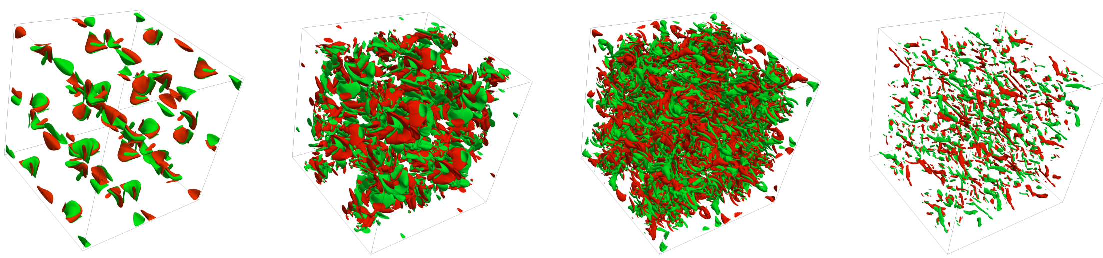

(a) Vortex roll-up (b) Coherent structure breakdown (c) Turbulence (d) Decay

FIG. 6. Time slots of the iso-surfaces of the z-component of the vorticity at 5.0s (a), 8.0s (b), 12.1s (c), 19.0s (d).

The time evolution of the z-component of the vorticity is illustrated in Fig. 6. As can be seen, the vortex roll-up happens in the early stage followed by stretch and breakdown of these vortex while preserving laminar property. Laminar turbulence transition is then observed, and the coherent structures are developed to fully turbulence structures. At the end of the flow evolution, the turbulence is dissipated. These results compare very favourably to the results of Tayyab *et al*.[25] which are performed using a classical pressure-based method.

In order to quantitatively analyze the viscous effect, the overall kinetic energy and its dissipation rate are evaluated in the next. The dissipation rate is of great importance because it's associated with the stress tensor. The overall kinetic energy is defined as the integral of the of kinetic energy over the whole domain, and the dissipation rate of kinetic energy is the temporal derivative of the overall kinetic energy, i.e.,

$$\kappa(t) = \frac{1}{2}\int_V (u_x^2 + u_y^2 + u_z^2)dV \qquad \varepsilon(t) = \frac{\partial\kappa(t)}{\partial t} \tag{18}$$

where the u_i are the velocity components with $i \in (x,y,z)$ and $\int_V$ is the integration over the whole domain. Fig. 7 shows the time evolution of these two normalized quantities. Excellent agreements

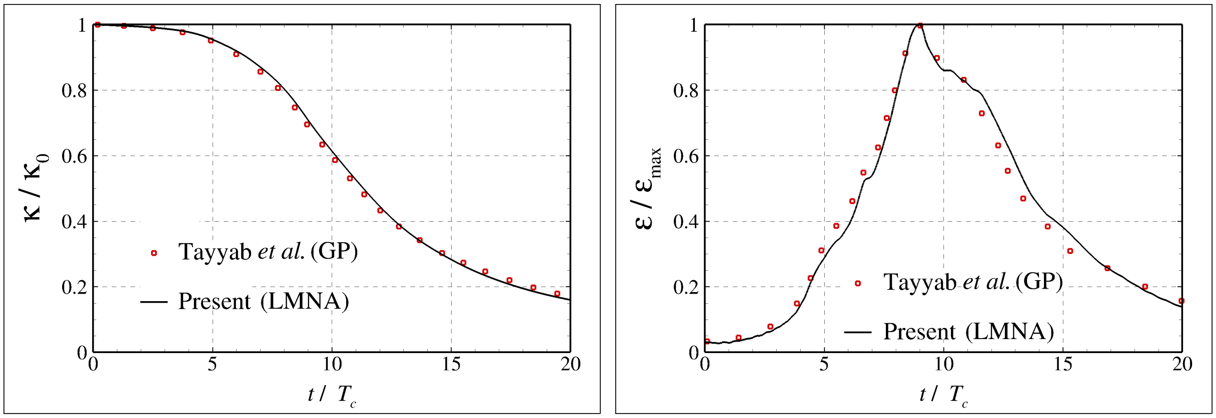

(a) Kinetic energy (b) Kinetic dissipation rate

FIG. 7. Kinetic energy (a) and kinetic dissipation rate (b) evolution. $T_c = 1$s, the kinetic energy and its dissipation rate are normalized respectively by the initial value and maximum value of corresponding quantity.

are obtained compared to the results of reference of Tayyab *et al.*[25]. Furthermore, the x and y-components of the velocity profile at the central line are plotted at time $12.11T_c$ in Fig. 8. The LMNA results match very well the solution of reference[25]. In addition, even the small turbulent structures are well captured by the LMNA, as shown on the x-component of the velocity in Fig. 8(a). All theses results show that the present LMNA method is able to simulate turbulent flow and laminar turbulence transition processes while keeping high computational efficiency.

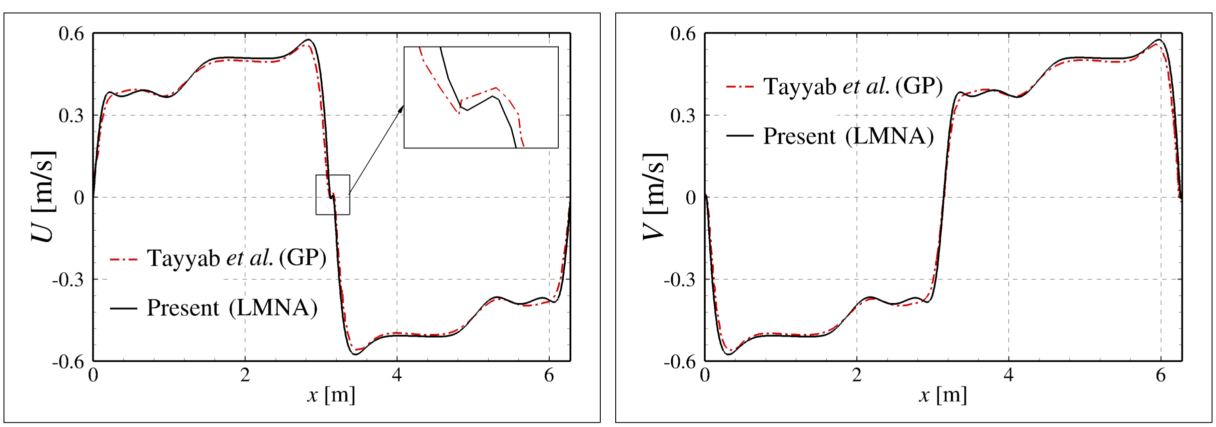

(a) Velocity x component (b) Velocity y component

FIG. 8. Profiles of x (a) and y (b) components of velocity at time $t = 12.11T_c$.

E. Flow around a circular heated cylinder at Reynolds number 3900

This section is dedicated to study the flow passing through a cylinder at Reynolds number Re $= 3900$ with isothermal solid wall in order to assess the capability of the present method in the LES (Large Eddy Simulation) framework[48]. A mesh convergence study is conducted firstly on an isothermal case where the temperature of solid wall is the same as the inflow. The results are benchmarked with experiments[49] and DNS (Direct Numerical Simulation)[50]. In addition, the LES results reported by[51,52] are also included to give a reference. Then, the thermal case is investigated with temperature difference between the solid wall and the inflow of $\Delta T = 300$K. The thermal effects on the flow features and turbulent heat flux are studied comparing with the LES results of Sircar *et al.*[51] and Jogee *et al.*[52]. In this study, we focus on the near wake region, for which a variety of experimental and numerical results are available in the literature for validation.

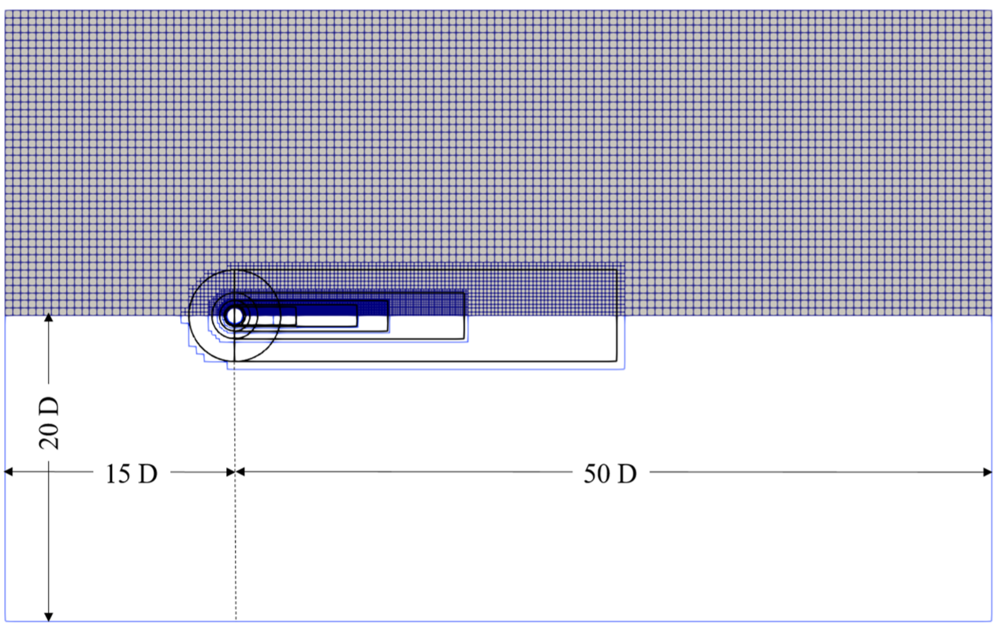

FIG. 9. Sketch of the grid refinement in the $x-y$ plane with seven levels of grid refinement. Black and blue lines show respectively the refinement boxes and the edges of each grid level.

1. Numerical setup

The sketch of the computational domain is shown in Fig. 9 together with the mesh. The cylinder has a diameter of $D = 0.01$m, and its center is chosen as the origin. The x, y, z directions are respectively the streamwise, transverse and spanwise direction regarding the inflow. The mesh in the transverse and spanwise directions as well as boundary conditions are symmetric with a spanwise extension of $L_z = 3D$ which is closed to the conventional $L_z = \pi D$ adopted by most LES studies[49,51–54]. The transverse width is $L_y = 20D$ for each side, and the distances to the inlet and outlet are respectively equal to 15 and 50 diameters, which is sufficiently large to reduce the effects of spurious pressure wave reflecting from the boundary. The inlet velocity and temperature boundary conditions are constant equal to $U_\infty = 5.968$ m s^{-1} and $T_\infty = 300$ K, respectively. Zero pressure gradient boundary is used for the outlet, and symmetric transverse top and bottom wall. Periodic boundary condition is provided in the spanwise direction. Isothermal no-slip boundary condition is imposed at the cylinder with two values of temperature equal to $T_w = 300$ K and $T_w = 600$ K to study the impact of the heat transfer.

Details on the grid refinement and related numerical parameters adopted in this study are given in Table. I. As Cartesian mesh is adopted by LBM, the mesh size is divided by a factor 2 for each grid refinement with the coarsest mesh size $\Delta x_{max}/D = 0.5$. The block refinement is the combination of cylinders and cuboids, as can be seen in Fig. 9 (cycle and rectangular for the 2D illustration). Three resolutions are chosen for this mesh convergence study with six, seven and eight grid levels. The number of mesh points are respectively equal to 1.88 millions, 6.52 millions and 25.16 millions. The finest grid sizes normalized by the cylinder diameter distributed along the isothermal cylinder wall are correspondingly $\Delta x_{min}/D = 1.56 \times 10^{-2}$, $\Delta x_{min}/D = 7.81 \times 10^{-3}$ and $\Delta x_{min}/D = 3.91 \times 10^{-3}$. The numbers of iterations required for a dimensionless time $U_\infty t^*/D = 1$ are 1115, 2227 and 4464, respectively, that corresponds to CPU times (by hour) of 1.44, 30.7 and 194.68, respectively. In order to obtain statistically converged results, 500 FOT (Flow Over Time), .i.e, $t = 500t^*$ (around 100 vortex shedding cycles) is chosen as initial transient time. Then the turbulent statistics and mean flow validation are realized from data collected over 150 FOT, i.e., $t = 150t^*$ (around 30 vortex shedding cycles). In this section, brackets $\langle \cdot \rangle$ and $(\cdot')$ denote time-averaged quantities and the corresponding fluctuations, respectively.

For compressible flows, the Favre-filtering is more convenient to avoid the SGS (Sub-Grid Scale) terms introduced in continuity equation[55,56]. A Vreman sub-grid scale model is adopted[57] with the model constant $C_s = 0.18$. A constant turbulent Prandtl number is chosen equal to $Pr_t = 0.85$ as suggested[51,52,58].

TABLE I. Details of meshes and computational setup, $t^* = D/U_\infty = 1.68 \times 10^{-3}$ s is the FOT (Flow Over Time) and it's used as a dimensionless quantity.

	Mesh	Total cell points (M)	Grid level	$\Delta x_{min}/D$	$\Delta t_{min}/t^*$	CFL_{u+c}	$t_w(h)$
	Coarse	1.88	6	1.56×10^{-2}	8.97×10^{-4}	0.684	1.44
Isotherm	Middle	6.52	7	7.81×10^{-3}	4.49×10^{-4}	0.684	30.7
	Fine	25.16	8	3.91×10^{-3}	2.24×10^{-4}	0.684	194.68
Non-isotherm	Fine	25.16	8	3.91×10^{-3}	4.49×10^{-4}	0.84	44.26

2. *Isothermal results at* $\Delta T = 0$ *K*

It's observed by Parnaudeau *et al*.[49] that the main flow features and turbulent characteristics in the wake region is determined by the re-circulation length L_{rc}, especially the transverse velocity and Reynolds stress. The length of this re-circulation bubble is defined as the distance from the rear stagnation point of the cylinder to the position where the sign change of the mean streamwise velocity along the centerline in the wake region. So the grid convergence study is focused on the prediction of this re-circulation zone.

The mean streamwise velocity $\langle u \rangle$ normalized by the inlet velocity U_∞ and the streamwise Reynolds stress $\langle u'u' \rangle$ normalized by U_∞^2 are plotted in Fig. 10. The negative mean velocity corresponds to the re-circulation zone as shown in Fig. 10(a). The overestimated re-circulation length obtained by the coarse mesh simulation pushes the streamwise Reynolds stress to the downstream direction compared to the experimental data by Parnaudeau *et al.*[49]. The results obtained with the middle mesh agree well with experimental data, except visible discrepancy of the maximum value of mean velocity in the re-circulation region. Finally, an excellent agreement is achieved with the fine mesh. In particular, the present LMNA result gives a re-circulation length L_{rc}/D equal to 1.46, compared to 1.51 given by Parnaudeau *et al.*[49] and 1.47 given by Dong *et al.*[50] that corresponds to an error of around 3% and less than 1%, respectively (see in Table II).

In the next, details of the flow features obtained for the finest mesh for the isothermal case

TABLE II. Experimental and numerical results of the literature together with present LMNA results. EXP stands for experiment.

Case	Model	$-Cpb$	$\langle C_d \rangle$	St	L_{rc}/D
Parnaudeau *et al.*[49]	EXP (PIV)	—	—	0.208	1.51
Dong *et al.*[50]	EXP (PIV)	—	—	0.212	1.47
Norberg *et al.*[59,60]	EXP (Multiple)	0.85-0.95	0.93-1.05	0.21	1.4-1.6
Ma *et al.*[61]	DNS (case II)	0.84	—	0.219	1.59
Dong *et al.*[50]	DNS	0.93-1.04	—	0.206-0.210	1-1.18
Lysenko *et al.*[53]	LES	0.91	0.97	0.209	1.67
Mani *et al.*[54]	LES	0.86	0.99	0.206	—
Franke and Frank *et al.*[62]	LES	0.85-0.94	0.978-1.005	0.209	1.34-1.64
Kravchnko and Moin *et al.*[63]	LES	0.94	1.04	0.210	1.35
Parnaudeau *et al.*[49]	LES	—	—	0.208	1.56
Jogee *et al.*[49]	LES	—	—	—	1.68
Sircar *et al.*[51]	LES	0.91	1.048	0.221	1.48
Coarse mesh	LES	0.81	1.06	0.212	1.67
Middle mesh	LES	0.86	1.04	0.223	1.41
Fine mesh	LES	0.84	1.04	0.223	1.46
Fine mesh (non-isothermal)	LES	0.79	1.00	0.212	1.69

are discussed including the mean flow, the turbulent characteristics and some aerodynamic coefficients.

Fig. 11 shows the laminar and turbulent structures of the flow. At this Reynolds number, the flow remains laminar along the cylinder wall and close to the cylinder just after the boundary layer separation. Large scale vortices develop at around two diameters from the rear stagnation point and are convected by the mean flow thus shedding alternatively from the upper and lower shear layers forming the well-known Von Karman street. The instability of the shear layer contributes to

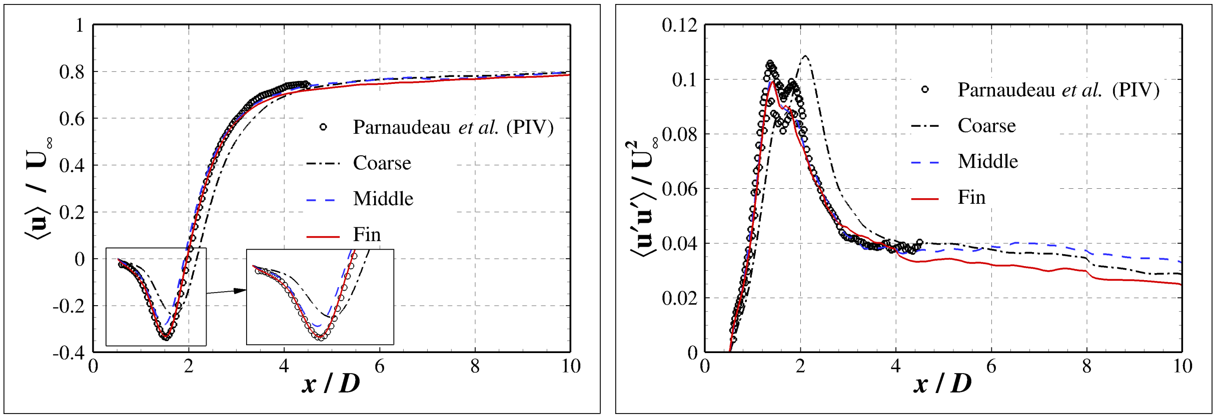

(a) Mean streamwise velocity profile

(b) Streamwise Reynolds stress profile

FIG. 10. Impact of grid refinement on the mean streamwise velocity (a) and streamwise Reynolds stress (b) distributions along the centerline in the wake region. PIV case I and II in the Ref.[49] are given in these figures.

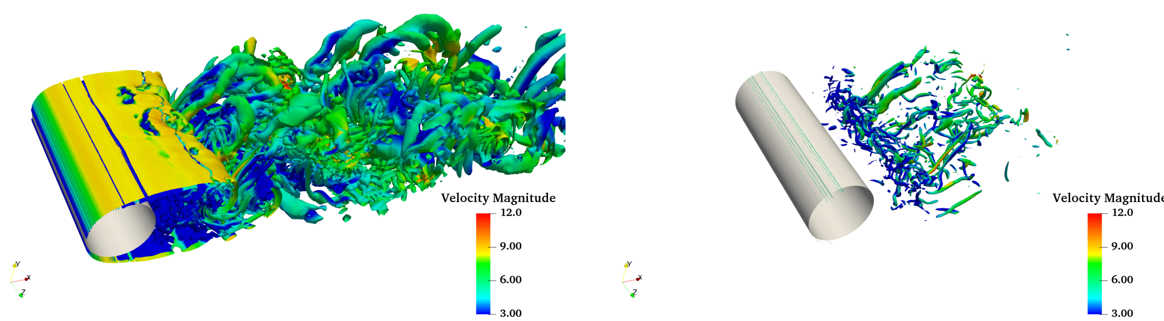

(a) $Q(D^2/U_\infty^2) = 1$

(b) $Q(D^2/U_\infty^2) = 100$

FIG. 11. Instantaneous iso-surfaces of the Q criterion $Q^* = Q(D^2/U_\infty^2) = 1$ (a), and $Q(D^2/U_\infty^2) = 100$ (b), colored by the velocity magnitude.

the laminar-turbulent transition. Thus, the large scale vortices break down to small scale vortices in the wake region.

Fig. 12 shows the time-averaged velocity field and the associated streamlines. As expected, the mean flow is globally symmetric to the axial line in the *xy*-plane, indicating that the solution is convergence over the computational time. The re-circulation zone is confined within the top and bottom shear layers. Two transverse lines in the re-circulation region at positions $X/D = 1.06$ and $X/D = 1.54$ are probed where the shear layer dynamics and turbulent statistics are quantitatively analyzed.

As shown in Fig. 13(a) and Table. II, compared to the experimental results of Parnaudeau

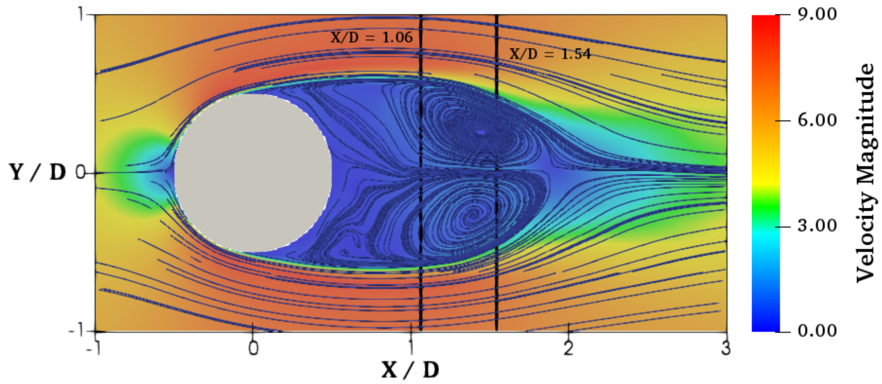

FIG. 12. Streamlines and velocity field of the mean flow at $Re = 3900$. Isothermal case.

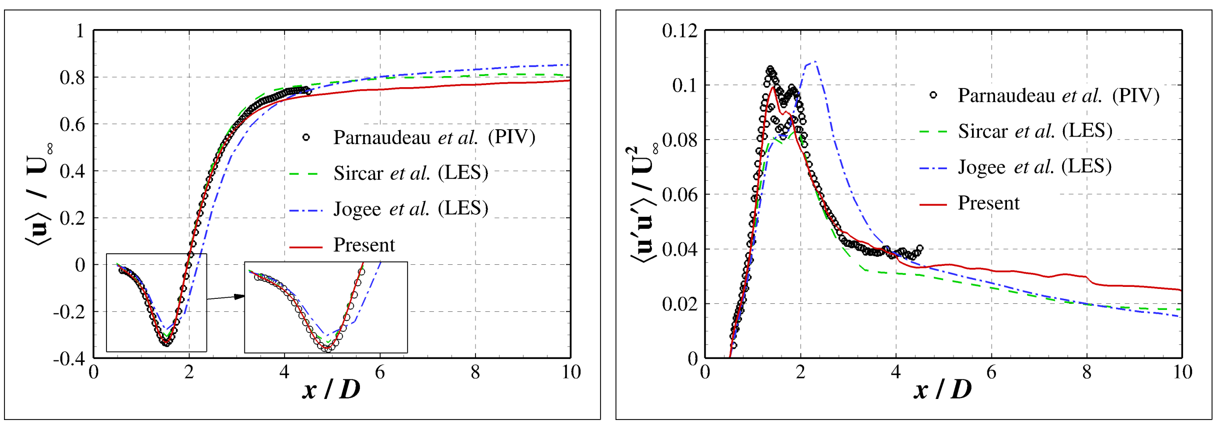

(a) Mean streamwise velocity profile

(b) Streamwise Reynolds stress profile

FIG. 13. Mean streamwise velocity (a) and streamwise Reynolds stress (b) distributions along the centerline in the wake region. PIV case I and II are provided from ref.[49]. LES results of Sircar *et al*.[51] and Jogee *et al*.[52] are also included.

et al.[49], the re-circulation length is correctly estimated by Sircar *et al*.[51] with $L_{rc,sircar}/D = 1.48$ and by the present LMNA with $L_{rc,present}/D = 1.46$. However, the overestimation of Jogee *et al*.[52] results in overestimating the peak value of the mean streamwise Reynolds stress $\langle u \rangle / U_\infty$, and in shifting the profiles of these quantities to the downstream direction. Moreover, the peak values of the mean streamwise velocity and corresponding Reynolds stress given by the present LMNA are closest to the experimental data. Furthermore, even in the relatively far wake region, i.e., $x/D \in [2.5, 4.5]$, present method gives best agreement with the experimental data. The far wake region, i.e., $x/D > 4.5$, won't be intensively studied in this investigation because of the lack of experimental results.

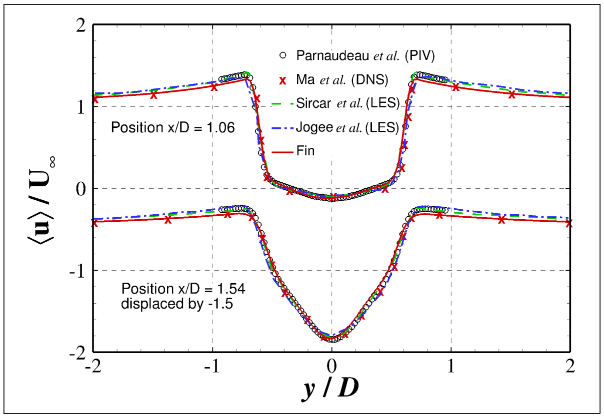

(a) Mean streamwise velocity profile

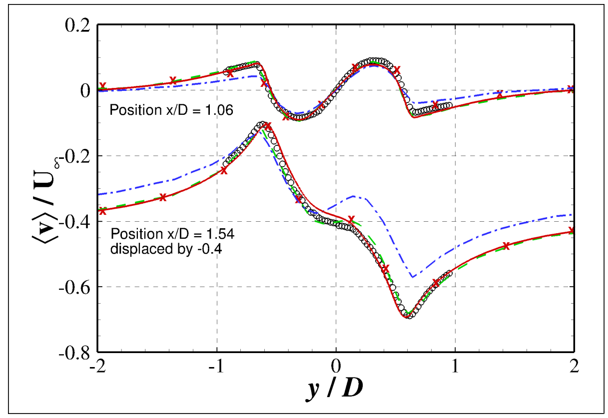

(b) Mean transverse velocity profile

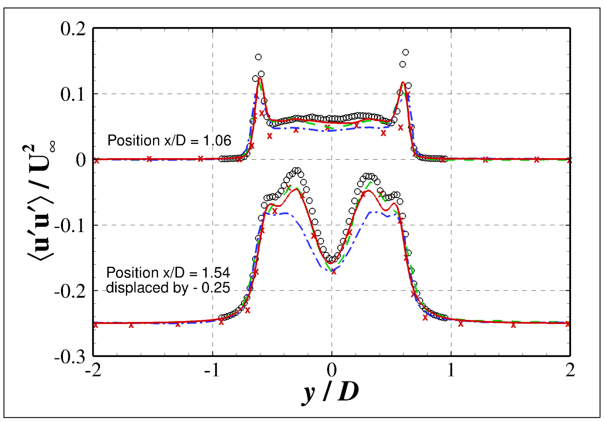

(c) Streamwise Reynolds stress distribution

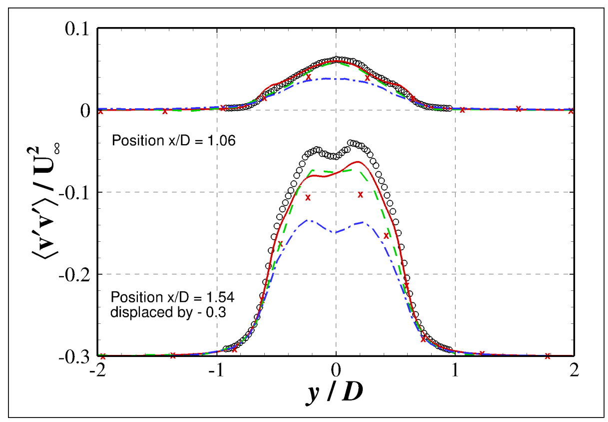

(d) Transverse Reynolds stress distribution

FIG. 14. (a, b) Mean streamwise and transverse velocity components. (c, d) Streamwise and transverse Reynolds stress components at position $x/D = 1.06$ and 1.54. The reference data from experiments PIV case II of Parnaudeau *et al*.[49] and DNS case II of Ma *et al*.[61] are included for comparison.

The normalized mean streamwise and transverse velocity $\langle u \rangle / U_\infty$ and $\langle v \rangle / U_\infty$ profiles and normalized streamwise and transverse Reynolds stress $\langle u'u' \rangle / U_\infty^2$ and $\langle v'v' \rangle / U_\infty^2$ at the two probe lines in the near wake region are shown in Fig. 14. As can be seen, the variation of these profiles are concentrated on the re-circulation region, i.e., $y/D \in [-0.8, 0.8]$. The disturbance outside this region is negligible. Hence the velocity tends to the inflow velocity profile and the turbulent statistics tends to zero. The mean streamwise velocity has the well-known U-shaped profile at $x/D = 1.06$ close to the cylinder boundary, and tends to a V-shaped profile as the probe moves to downstream direction at $x/D = 1.54$. Contrary to the symmetric form of mean streamwise velocity profile, the mean transverse velocity profile is anti-symmetric with respect to the axial line. Regarding the transverse quantities like the transverse mean velocity component (Fig. 14(b)) and the transverse

Reynolds stress component (Fig. 14(d)), the discrepancy with the results of the literature is larger. The deviation of Jogee's results are very significant compared to the experimental[49] and DNS[61] data. However, the discrepancy between the present LMNA results and the LES results of Sircar *et al.*[51], or the experimental[49] and DNS[61] results is rather small.

The streamwise Reynolds stress profiles show two peaks (Fig. 14(c)) which correspond to the detached shear layers. The instability induced by shear phenomena produces highest perturbation near the shear layers. The streamwise Reynolds stress are three times larger at the shear layer than the values in the center of the re-circulation bubble. The two peaks show a diffusive trend as the probe moves downstream, which is probably influenced by the oscillations of the alternative vortex shedding phenomena. The values of the transverse Reynolds stress components are around three times larger than the streamwise ones in the center of the re-circulation bubble because of the oscillations in the transverse direction of the vortex shedding phenomena.

3. *Non-isothermal results at* $\Delta T = 300K$

The cylinder is now heated to $T_w = 600$ K. In order to investigate the influence of heat transfer on the flow features, the turbulent heat flux and temperature fluctuations are analyzed quantitatively at the same probe locations as in previous section. The non-isothermal LES results of Sircar *et al*.[51] and Jogee *et al*.[52] at the same temperature difference $\Delta T = 300$ K are included as references. The fine mesh defined in former section is used for the non-isothermal simulations here. The time step is fixed at $\Delta t^* = 4.49 \times 10^{-4}$. Let's notice that similar computations with the fully compressible solver requires a time step 16.4 times smaller equal to $\Delta t^* = 2.74 \times 10^{-5}$.

TABLE III. Recirculation lengths for the isothermal and the non-isothermal cases. Present LMNA results are given together with LES predictions of the literature by Sircar *et al.*[51] and Jogee *et al.*[52].

Case	L_{rc}/D		Bubble length change (%)
	Isothermal	$\Delta T = 300K$	
Jogee *et al.*[52]	1.68	2.04	21.4
Sircar *et al.*[51]	1.480	1.606	8.5
Current	1.46	1.69	15.8

Table III shows that the re-circulation bubble length becomes larger when the cylinder is heated. This is probably caused by the temperature increase in the detached shear layer. As can be seen in the time-averaged temperature field in Fig. 15(b), the temperatures of the shear layer and of the re-circulation zone are higher than elsewhere. These local temperature elevations lead to a change of density and viscosity, and hence results in a lower local Reynolds number. Consequently, the laminar laminar-turbulent transition is delayed downstream that leads to a larger re-circulation bubble.

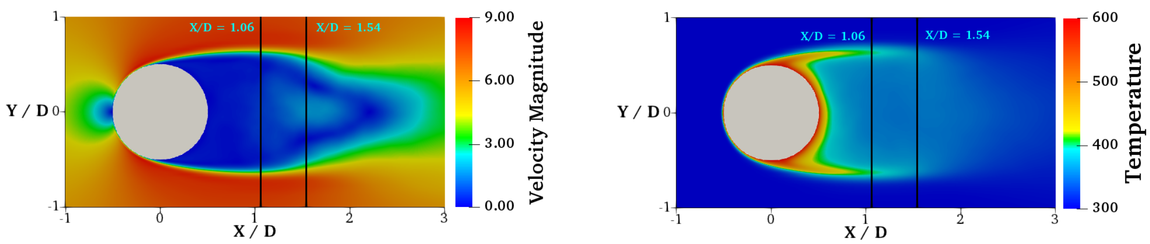

(a) Mean velocity

(b) Mean temperature

FIG. 15. Color maps of the mean velocity magnitude (a) and temperature (b).

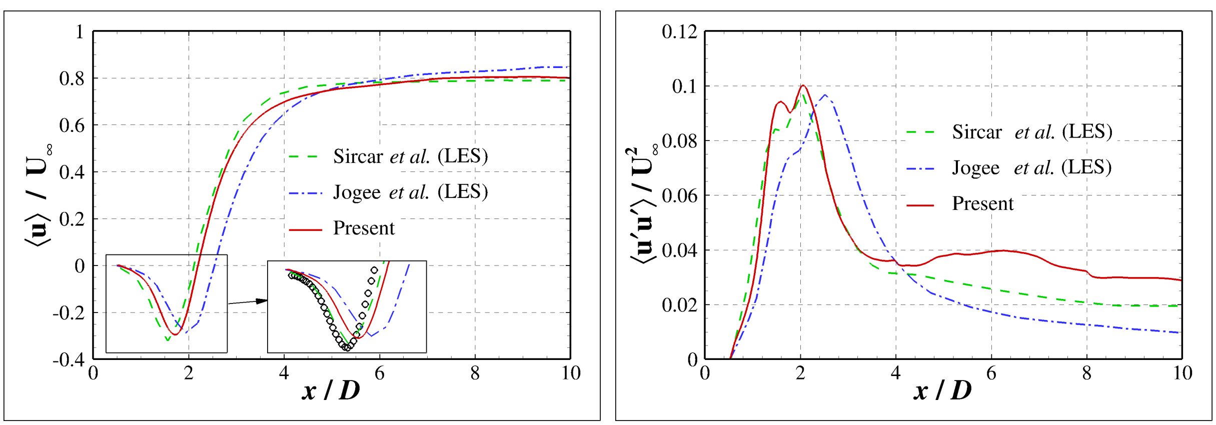

(a) Mean streamwise velocity profile

(b) Streamwise Reynolds stress profile

FIG. 16. Profiles along the centerline in the wake region of the mean streamwise velocity (a) and streamwise Reynolds stress (b) components. Non-isothermal LES results of Sircar *et al.*[51] and Jogee *et al.*[52] at the same temperature difference $\Delta T = 300$ K are included as references.

Compared to the isothermal simulations, the bubble length is increased of 21.4 % and 8.5 % for Jogee *et al.*[52] and Sircar *et al.*[51], respectively, indicating that the Jogee's LES results are more sensitive to the thermal effects than the Sircar ones. In the present simulation the increase is of 15.8%. However, as the isothermal bubble length predicted by the Jogee's LES results was already

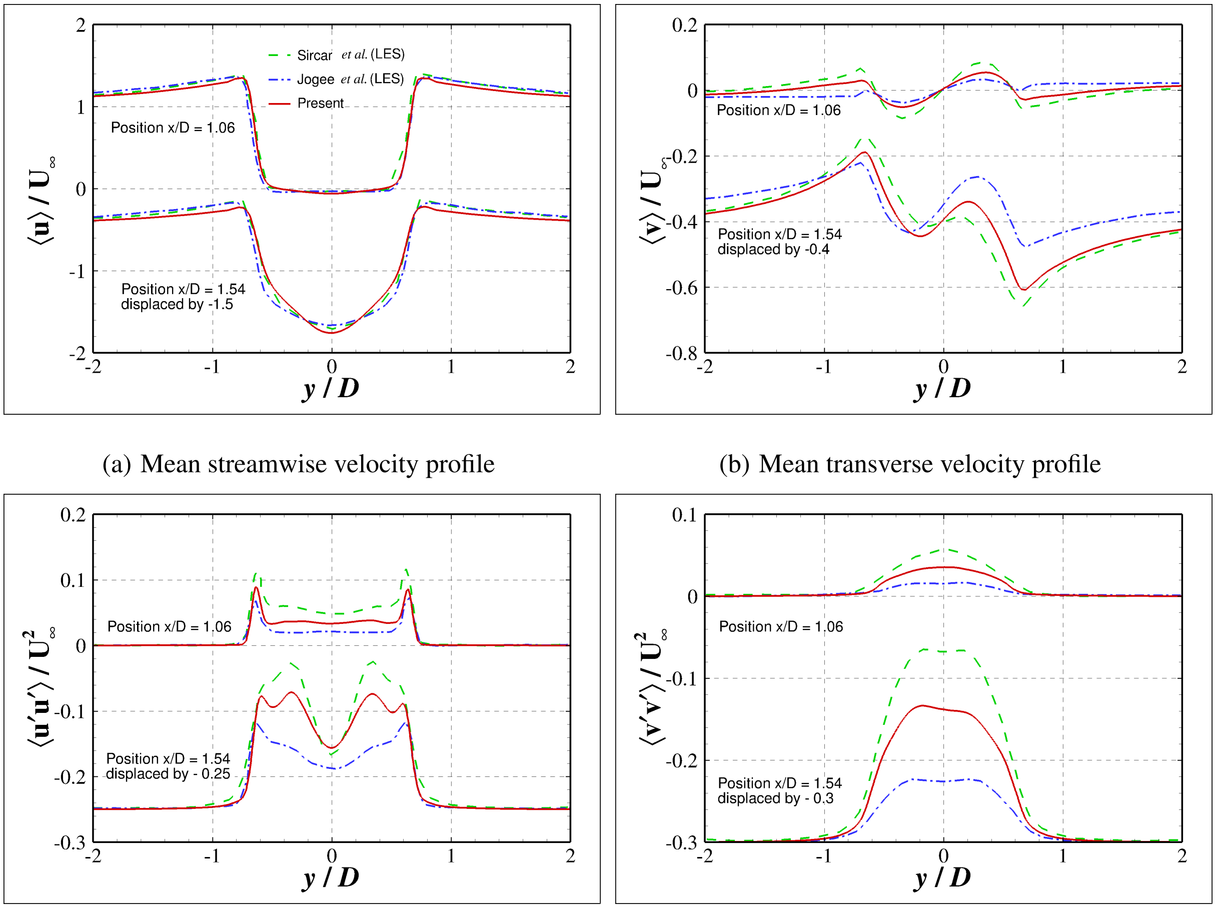

(a) Mean streamwise velocity profile

(b) Mean transverse velocity profile

(c) Streamwise Reynolds stress distribution

(d) Transverse Reynolds stress distribution

FIG. 17. Mean streamwise and transverse velocity components (a, b), streamwise and transverse Reynolds stress components (c, d) at $x/D = 1.06$ and 1.54. Non-isothermal LES results of Sircar *et al.*[51] and Jogee *et al.*[52] at the same temperature difference $\Delta T = 300$ K are included as references.

11% larger than the experimental data of reference, the bubble length predicted by the Jogee's non-isothermal LES is closed to $L_{rc,Jogee}/D = 2.04$, which is much larger than the values predicted by Sircar *et al.* and by the present method. This difference in the bubble length is clearly visible on Fig. 16. Despite the two times larger bubble length change predicted by the present method compared to Sircar *et al.*, the thermal re-circulation length is quite close and the discrepancy of the turbulent characteristics is also small in the near wake region.

The mean flow profiles and Reynolds stress at the same probe locations show the turbulent flow feature modification caused by thermal effects in Fig. 17. As can be seen, by comparing the velocity profiles of Fig. 14, the mean streamwise velocity profiles at $x/D = 1.06$ are quite close to the isothermal ones. However the profiles at $x/D = 1.54$ change from a V-shape to a

U-shape because the relative positions of the probe lines with respect to the bubble length are pushed upstream due to the growth of the bubble length. This change is magnified for the mean transverse velocity profiles shown in Fig. 17(b), especially at $x/D = 1.54$. As can be seen, the mean transverse velocity component in the isothermal case at $x/D = 1.54$ shows a monotonous drop from $y/D = -0.6$ to $y/D = 0.6$. However, all the transverse mean velocity profiles of the thermal cases change sign three times of which these profiles are more similar to the ones at $x/D = 1.06$.

The sensitivity with thermal effect of the turbulent statistics is shown in Fig. 17(c) and Fig. 17(d). Both the streamwise and transverse Reynolds stress profiles obtained by Sircar *et al.*[51] are very close to the isothermal results of Parnaudeau *et al.*[49]. This means that the results of Sircar *et al.*[51] are rather insensitive to thermal effects. In contrast, the results of Jogee *et al.*.[52] exhibit significant variations with respect to their isothermal results. Present results are between those of Sircar *et al.*[51] and Jogee *et al.*[52] but closer to Sircar *et al.*[51] results. This is consistent with the re-circulation bubble length change due to thermal effect, Table. III.

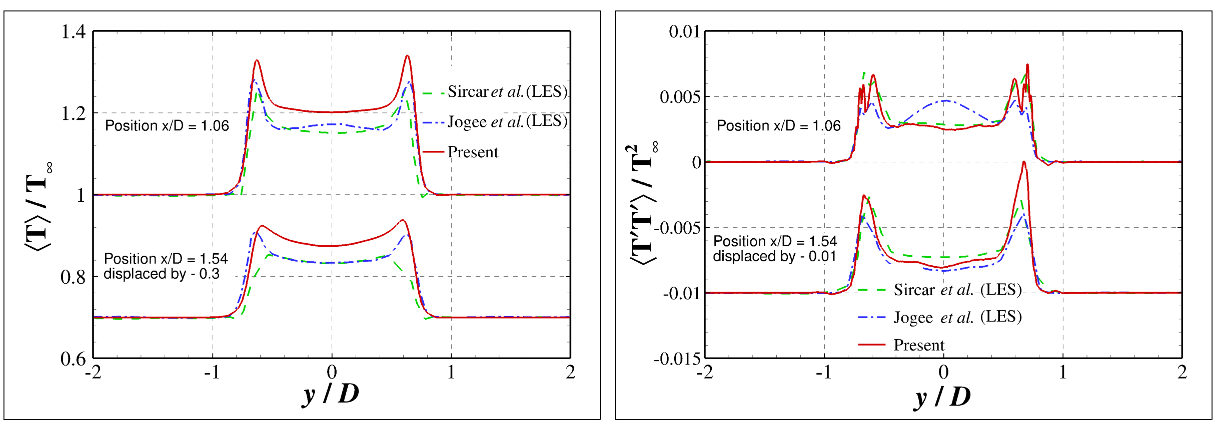

(a) Temperature profile

(b) RMS of Temperature fluctuation distribution

FIG. 18. Mean temperature profiles (a) and RMS of temperature fluctuations (b) at $x/D = 1.06$ and $x/D = 1.54$. Non-isothermal LES results of Sircar *et al.*[51] and Jogee *et al.*[52] at the same temperature difference $\Delta T = 300$ K are included as references.

In the next, the thermal characteristics including the temperature distribution and turbulent heat flux will be discussed. Fig. 18 shows the mean temperature profiles and the RMS (Root Mean Square) of temperature fluctuation $\langle T'T' \rangle / T_\infty^2$ distribution at the same probe lines. Similar to the streamwise Reynolds stress profiles, the mean temperature profiles and RMS distribution display the same features. Two peaks are located at the detached heated shear layers as shown in

Fig. 15(b). The temperature fluctuations peaks correspond to the peaks on the mean temperature profiles due to the temperature amplitude and the strong instability at the shear layers. In the present LMNA results, the mean temperature at the re-circulation bubble is slightly higher than the LES results of Sircar *et al.* and Jogee *et al.*, whereas the temperature fluctuations are very close. Fig. 19 shows the color map of the streamwise $\langle u'T' \rangle / U_\infty T_\infty$ and the transverse turbulent heat flux $\langle v'T' \rangle / U_\infty T_\infty$ where the positive (red) and negative (blue) zones are highlighted.

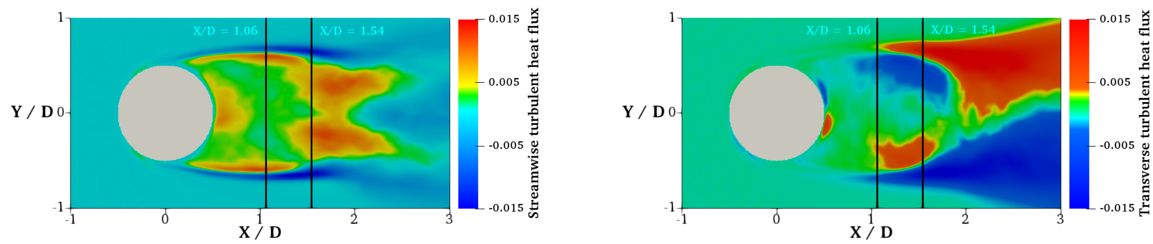

(a) Streamwise turbulent heat flux

(b) Transverse turbulent heat flux

FIG. 19. 2D color maps of the streamwise (a) and transverse (b) turbulent heat flux obtained with the present LMNA.

Fig. 20 shows the temperature fluctuations, and the streamwise heat flux distribution along the center line. As can be seen, the RMS of temperature fluctuations and turbulent heat flux attain a peak value near the rear point of the cylinder, showing that the thermal fluctuations are most significant at this position. The turbulent heat flux is positive in the re-circulation region, and switches to a negative value outside the re-circulation region. This means that the heat transfer is from the heated cylinder to the cold fluid in the re-circulation zone. The position where the turbulent heat flux becomes zero is very close to the margin of re-circulation zone, and this phenomenon is consistent for all the three LES results: $L_{rc,Sircar} < L_{rc,current} < L_{rc,Jogee}$.

The streamwise and transverse turbulent heat flux profiles along the two probe lines are plotted in Fig. 21. The heat transfer direction is represented by the sign of the turbulent heat flux. The steep gradient of temperature at the shear layer produces the four peaks of each profile with opposite sign near each other. This is consistent with the color map of Fig. 19, where the highlighted blue zone and red zone are distributed alternatively near the shear layer. Moreover, the transverse turbulent heat flux at center line ($y/D = 0$) is zero because the transverse velocity along the center line is zero inside the re-circulation region. Lastly, the discrepancy between the results of Sircar *et al.* and the present ones is not significant for both the peak values and the profile shapes. However, the deviation with the LES results of Jogee *et al.* is considerably larger, which is consistent with

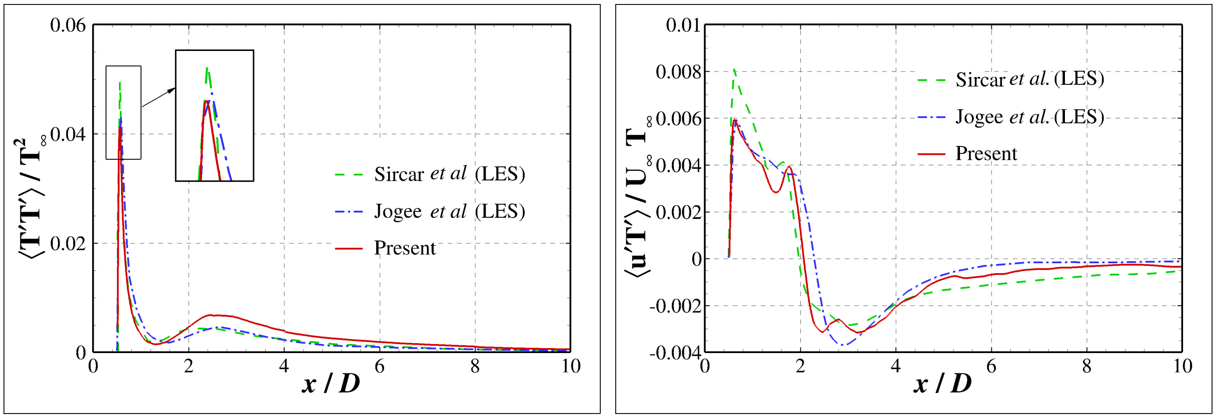

(a) (b)

FIG. 20. RMS of temperature fluctuations (a) and turbulent heat flux (b) profiles along the centerline in the wake.

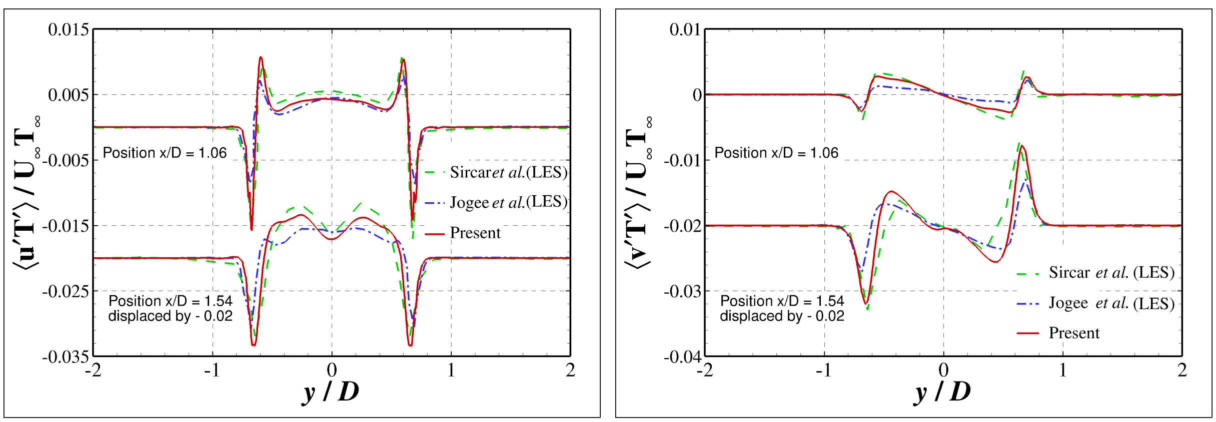

(a) (b)

FIG. 21. Streamwise (a) and transverse (b) turbulent heat flux profiles at $x/D = 1.06$ and $x/D = 1.54$.

previous description. It is probably due to the weaker influence of the thermal effects on the flow features.

These results show that the new LMNA provides promising results for complex turbulent isothermal configurations and consistent explanation for heat transfer problems with large temperature differences. Moroever, with a time step more than 15 times larger than for a fully compressible LBM solver, the computational efficiency is strongly improved.

IV. CONCLUSION

In this paper, we have proposed a new hybrid Lattice Boltzmann method for dealing efficiently with Low Mach thermal flows. To overcome the time step constraint of the fully compressible LBM solvers due to acoustic waves, the low-Mach number approximation has been considered and adapted to the compressible hybrid LBM solver developed by the team[37]. The present algorithm overcomes the drawback of the PGS method related to the modification of the pressure gradient. In addition, the present algorithm can be easily implemented to improve any density based or pressure based compressible solvers, which makes it more flexible than other existing LB algorithms based on LMNA.

The performance of present method are assessed by two classes of cases. The first category of test scenarios includes flows in laminar regime, i.e., one dimensional gravity column, 2D rising thermal bubble and 2D natural convection for which all the results agree well with the reference. The second category consists of 3D Taylor Green Vortex and 3D flow passing through a heated cylinder in turbulent regime. Excellent agreements are obtained especially on the average flow features with respect to reference results of the literature. Some discrepancies are observed for the turbulent quantities of 3D heated cylinder compared to other LES results. The results of present method are between the LES results of Sircar *et al*.[51] and Jogee *et al*.[52] and closer to the one of Sircar. This indicates that current solution is more sensible to the turbulent thermal effect than Sircar *et al*.[51] and less sensible than Jogee *et al*.[52]. This disparity is most likely due to the differences in turbulent models and mesh configurations adopted in these LES investigations. Furthermore, table IV summarizes the computing speed-ups of all the test cases employed in this investigation. As can be seen, the computational efficiency is increased by at least a factor of ten.

ACKNOWLEDGEMENTS

This work was performed within ProLB solver. Centre de Calcul Intensif d'Aix-Marseille is acknowledged for granting access to its high performance computing resources. We also acknowledge the supports of ANR, Renault, Airbus and SafranTech by the Industrial Chair Program ALBUMS (ANR-CHIND-18-ALBUMS).

TABLE IV. Computations speedup for the different test cases of the paper. The speedup is evaluated with respect to fully compressible LBM computations.

Test cases	Speedup
1D Gravity column at $\mathrm{Ma} = \frac{\sqrt{gL}}{c} \approx 0.029$	10.0
2D Rising bubble at Ma = 0.018	25.0
2D Natural convection at Ma = 0.0035	55.6
3D Taylor Green Vortex at Ma = 0.0029	70.3
3D Heated cylinder at Ma = 0.017	16.4

Appendix A: The low Mach number approximation of the Navier-Stokes equations

The low-Mach number acceleration strategy based on the scaling of fully compressible Navier-Stokes equations in low-Mach number limit is presented in this section. One of the main challenges when simulating low-Mach number thermal flows using a compressible solver is to keep high computational efficiency despite the non-dominant acoustic scale fluctuations. A method to cure this issue is based on a scale analysis, which divides the fully compressible Navier-Stokes equations by a leading order fluctuations thermal dynamics and a non-dominant acoustic scale.

Based on the asymptotic analysis, any variable ϕ appears in the fully compressible Navier-Stokes system will be expanded as

$$\phi = \phi^0 + \varepsilon \phi^h + \mathscr{O}(\varepsilon^2) \tag{A1}$$

with

$$\varepsilon \equiv \gamma_\infty \mathrm{Ma}_\infty^2 \ . \tag{A2}$$

Then, the leading order Navier-Stokes equations read[2]

$$\frac{\partial \rho}{\partial t} + \frac{\partial \rho u_\alpha}{\partial x_\alpha} = 0 \,, \tag{A3a}$$

$$\frac{\partial p}{\partial x_\alpha} = 0, \tag{A3b}$$

$$\frac{\partial \rho u_\alpha}{\partial t} + \frac{\partial \rho u_\alpha u_\beta}{\partial x_\beta} = -\frac{\partial p^h}{\partial x_\alpha} + \frac{1}{\mathrm{Re}_\infty}\frac{\partial \Pi_{\alpha\beta}}{\partial x_\beta} + \frac{1}{\mathrm{Fr}_\infty^2}\rho g_\alpha \,, \tag{A3c}$$

$$\rho T \left(\frac{\partial s}{\partial t} + u_\alpha \frac{\partial s}{\partial x_\alpha} \right) = -\frac{1}{\mathrm{Re}_\infty \mathrm{Pr}_\infty}\frac{\partial q_\alpha}{\partial x_\alpha} \,, \tag{A3d}$$

$$p = \rho r T \;, s = c_v \ln \frac{p}{\rho^\gamma} \,. \tag{A3e}$$

Together with the reference Reynolds, Froude and Prandtl numbers

$$\mathrm{Re}_\infty \equiv \frac{\rho_\infty u_\infty x_\infty}{\mu_\infty} \,, \quad \mathrm{Fr}_\infty \equiv \frac{u_\infty}{\sqrt{g_\infty x_\infty}} \,, \quad \mathrm{Pr}_\infty \equiv \frac{c_{p_\infty} \mu_\infty}{\lambda_\infty} \,, \tag{A4}$$

In the above system, the thermodynamic pressure p is spatial independent according to equation (A3b). Also, one additional equation for the hydrodynamic pressure p^h is necessary to resolve this set of equations. Typically, this is achieved through a Poisson equation constructed from the mass and momentum equations[64].

Appendix B: Thermodynamic pressure in a closed system

The equation of state $s = c_v \ln \frac{p}{\rho^\gamma}$ gives the following derivative relationship

$$ds = \frac{c_v}{p} dp - \frac{c_p}{\rho} d\rho \,. \tag{B1}$$

In a closed system, the global mass of the system should be conserved, i.e.

$$\int \frac{\partial \rho}{\partial t} dV = 0 \,, \tag{B2}$$

together with equation (B1), the spatial independent thermodynamic pressure can be calculated by

$$\frac{dp}{dt} = \frac{\int \left(\frac{\rho}{c_p} \frac{\partial s}{\partial t} \right) dV}{\int \frac{\rho}{\gamma p} dV} \,. \tag{B3}$$

[2] The superscript 0 for the variables with $0^t h$ order is neglected here.

REFERENCES

[1]Gordon Draisey Mallinson and G De Vahl Davis. Three-dimensional natural convection in a box: a numerical study. *J Fluid Mech.*, 83:1–31, 1977.

[2]Gray DD and Giorgini A. The validity of the Boussinesq approximation for liquids and gases. *Int J Heat Mass Transfer*, 19:545–51, 1976.

[3]Frohlich J., Laure P., and Peyret R. Large departures from Boussinesq approximation in the Rayleigh-Bénard problem. *Phys Fluids A*, 4:1355–72, 1992.

[4]Paolucci S. *On the filtering of sound from the Navier–Stokes equations.*, volume 82. Technical Report, Sandia National Laboratories USA SAND, 1982.

[5]J.D. Ramshaw, P.J. O'Rourke, and L.R. Stein. Pressure gradient scaling method for fluid flow with nearly uniform pressure. *Journal of Computational Physics*, 58(3):361–376, may 1985.

[6]Yi Wang and Arnaud Trouvé. Artificial acoustic stiffness reduction in fully compressible, direct numerical simulation of combustion. *Combustion Theory and Modelling*, 8(3):633–660, sep 2004.

[7]GP Zank and WH Matthaeus. Nearly incompressible hydrodynamics and heat conduction. *Physical review letters*, 64(11):1243, 1990.

[8]BJ Bayly, CD Levermore, and T Passot. Density variations in weakly compressible flows. *Physics of Fluids A: Fluid Dynamics*, 4(5):945–954, 1992.

[9]Pierre Sagaut and Claude Cambon. *Homogeneous turbulence dynamics*, volume 10. Springer, 2008.

[10]Chenoweth D.R. and Paolucci S. Natural convection in an enclosed vertical air layer with large horizontal temperature differences. *J Fluid Mech.*, 169:173–210, 1986.

[11]Bouloumou O.and Serre E., Bontoux P., and Fröhlich J. A 3D pseudo-spectral low Mach-number solver for buoyancy driven flows with large temperature differences. *Comp. Fluids*, 66:107–120, 2012.

[12]Timm Krüger, Halim Kusumaatmaja, Alexandr Kuzmin, Orest Shardt, Goncalo Silva, and Erlend Magnus Viggen. The Lattice Boltzmann method. *Springer International Publishing*, 10(978-3):4–15, 2017.

[13]Zhaoli Guo and Chang Shu. *Lattice Boltzmann method and its application in engineering*, volume 3. World Scientific, 2013.

[14]Yongliang Feng, Pierre Boivin, Jérôme Jacob, and Pierre Sagaut. Hybrid recursive regularized

thermal Lattice Boltzmann model for high subsonic compressible flows. *Journal of Computational Physics*, 394:82–99, 2019.

[15]Yongliang Feng, Pierre Sagaut, and Wen-Quan Tao. A compressible Lattice Boltzmann finite volume model for high subsonic and transonic flows on regular Lattices. *Computers & Fluids*, 131:45–55, 2016.

[16]T Coratger, G Farag, S Zhao, Pierre Boivin, and P Sagaut. Large-eddy Lattice-Boltzmann modeling of transonic flows. *Physics of Fluids*, 33(11):115112, 2021.

[17]Florian Renard, Yongliang Feng, Jean-François Boussuge, and Pierre Sagaut. Improved compressible hybrid Lattice Boltzmann method on standard Lattice for subsonic and supersonic flows. *Computers & Fluids*, 219:104867, 2021.

[18]G Farag, S Zhao, T Coratger, Pierre Boivin, G Chiavassa, and Pierre Sagaut. A pressure-based regularized Lattice-Boltzmann method for the simulation of compressible flows. *Physics of Fluids*, 32(6):066106, 2020.

[19]S Zhao, G Farag, Pierre Boivin, and P Sagaut. Toward fully conservative hybrid Lattice Boltzmann methods for compressible flows. *Physics of Fluids*, 32(12):126118, 2020.

[20]Yongliang Feng, Pierre Sagaut, and Wenquan Tao. A three dimensional Lattice model for thermal compressible flow on standard Lattices. *Journal of Computational Physics*, 303:514–529, 2015.

[21]Yong-Liang Feng, Shao-Long Guo, Wen-Quan Tao, and Pierre Sagaut. Regularized thermal Lattice Boltzmann method for natural convection with large temperature differences. *International Journal of Heat and Mass Transfer*, 125:1379–1391, 2018.

[22]Guanxiong Wang, Lincheng Xu, Eric Serre, and Pierre Sagaut. Large temperature difference heat dominated flow simulations using a pressure-based Lattice Boltzmann method with mass correction. *Physics of Fluids*, 33(11):116107, 2021.

[23]Jérôme Jacob, Orestis Malaspinas, and Pierre Sagaut. A new hybrid recursive regularised Bhatnagar–Gross–Krook collision model for Lattice Boltzmann method-based large Eddy simulation. *Journal of Turbulence*, 5248:1–26, 2018.

[24]Yongliang Feng, Muhammad Tayyab, and Pierre Boivin. A Lattice-Boltzmann model for low-Mach reactive flows. *Combustion and Flame*, 196:249–254, 2018.

[25]Tayyab Muhammad. Development of combustion modelling within Lattice Boltzmann framework. *Thesis*, 2020.

[26]Xiaoyi He, Shiyi Chen, and Gary D Doolen. A novel thermal model for the Lattice Boltzmann

method in incompressible limit. *Journal of computational physics*, 146(1):282–300, 1998.

[27]Zhaoli Guo, Baochang Shi, and Chuguang Zheng. A coupled Lattice BGK model for the Boussinesq equations. *International Journal for Numerical Methods in Fluids*, 39(4):325–342, 2002.

[28]Zhaoli Guo, Chuguang Zheng, Baochang Shi, and TS Zhao. Thermal Lattice Boltzmann equation for low Mach number flows: Decoupling model. *Physical Review E*, 75(3):036704, 2007.

[29]Q Li, KH Luo, YL He, YJ Gao, and WQ Tao. Coupling Lattice Boltzmann model for simulation of thermal flows on standard Lattices. *Physical Review E*, 85(1):016710, 2012.

[30]Andreas Meister. Asymptotic single and multiple scale expansions in the low Mach number limit. *SIAM Journal on Applied Mathematics*, 60(1):256–271, 1999.

[31]O Filippova and D Hänel. Lattice-BGK model for low Mach number combustion. *International Journal of Modern Physics C*, 9(08):1439–1445, 1998.

[32]Taehun Lee, Ching-Long Lin, and Lea-Der Chen. A Lattice Boltzmann algorithm for calculation of the laminar jet diffusion flame. *Journal of Computational Physics*, 215(1):133–152, 2006.

[33]Kazuhiro Yamamoto, Xiaoyi He, and Gary D Doolen. Simulation of combustion field with Lattice Boltzmann method. *Journal of statistical physics*, 107(1):367–383, 2002.

[34]Seyed Ali Hosseini, Hesam Safari, Nasser Darabiha, Dominique Thévenin, and Manfred Krafczyk. Hybrid Lattice Boltzmann-finite difference model for low Mach number combustion simulation. *Combustion and Flame*, 209:394–404, 2019.

[35]SA Hosseini, A Abdelsamie, N Darabiha, and D Thévenin. Low-Mach hybrid Lattice Boltzmann-finite difference solver for combustion in complex flows. *Physics of Fluids*, 32(7):077105, 2020.

[36]Yuhui Cao. Variable property-based Lattice Boltzmann flux solver for thermal flows in the low Mach number limit. *International Journal of Heat and Mass Transfer*, 103:254–264, 2016.

[37]G Farag, T Coratger, G Wissocq, S Zhao, Pierre Boivin, and P Sagaut. A unified hybrid Lattice-Boltzmann method for compressible flows: Bridging between pressure-based and density-based methods. *Physics of Fluids*, 33(8):086101, 2021.

[38]G. Farag, S. Zhao, G. Chiavassa, and P. Boivin. Consistency study of Lattice-Boltzmann schemes macroscopic limit. *Physics of Fluids*, 33(3):037101, 2021.

[39]Xiaoyi He, Gary D. Doolen, and T. Clark. Comparison of the Lattice Boltzmann method and the artificial compressibility method for Navier-Stokes equations. *Journal of Computational Physics*, 179(2):439–451, 2002.

[40]Alexandre Joel Chorin. A numerical method for solving incompressible viscous flow problems.

Journal of computational physics, 135(2):118–125, 1967.

[41] T. Coratger, G. Farag, S. Zhao, P. Boivin, and P. Sagaut. Large-eddy Lattice-Boltzmann modeling of transonic flows. *Physics of Fluids*, 33(11):115112, 2021.

[42] Jacques Salat, S Xin, Patrice Joubert, A Sergent, F Penot, and Patrick Le Quere. Experimental and numerical investigation of turbulent natural convection in a large air-filled cavity. *International Journal of Heat and Fluid Flow*, 25(5):824–832, 2004.

[43] S Mergui and F Penot. Convection naturelle en cavité carrée différentiellement chauffée: investigation expérimentale à Ra= 1, 69$\times$ 109. *International Journal of Heat and Mass Transfer*, 39(3):563–574, 1996.

[44] C Wan, BSV Patnaik, GW Wei, and D. A new benchmark quality solution for the buoyancy-driven cavity by discrete singular convolution. *Numerical Heat Transfer: Part B: Fundamentals*, 40(3):199–228, 2001.

[45] Nicola Massarotti, P Nithiarasu, and OC Zienkiewicz. Characteristic-based-split (CBS) algorithm for incompressible flow problems with heat transfer. *International Journal of Numerical Methods for Heat & Fluid Flow*, 1998.

[46] Jan Vierendeels, Bart Merci, and Erik Dick. Numerical study of natural convective heat transfer with large temperature differences. *International Journal of Numerical Methods for Heat & Fluid Flow*, 2001.

[47] Jan Vierendeels, Bart Merci, and Erik Dick. Benchmark solutions for the natural convective heat transfer problem in a square cavity with large horizontal temperature differences. *International Journal of Numerical Methods for Heat & Fluid Flow*, 2003.

[48] Pierre Sagaut. *Large Eddy simulation for incompressible flows: an introduction*. Springer Science & Business Media, 2006.

[49] Philippe Parnaudeau, Johan Carlier, Dominique Heitz, and Eric Lamballais. Experimental and numerical studies of the flow over a circular cylinder at Reynolds number 3900. *Physics of Fluids*, 20(8):085101, 2008.

[50] S Dong, GE Karniadakis, A Ekmekci, and D Rockwell. A combined Direct Numerical Simulation–Particle Image Velocimetry study of the turbulent near wake. *Journal of Fluid Mechanics*, 569:185–207, 2006.

[51] Arpan Sircar, Mark Kimber, Srujan Rokkam, and Gerrit Botha. Turbulent flow and heat flux analysis from validated Large Eddy simulations of flow past a heated cylinder in the near wake region. *Physics of Fluids*, 32(12):125119, 2020.

[52]Sourabh Jogee, BVSSS Prasad, and Kameswararao Anupindi. Large-Eddy simulation of non-isothermal flow over a circular cylinder. *International Journal of Heat and Mass Transfer*, 151:119426, 2020.

[53]Dmitry A Lysenko, Ivar S Ertesvåg, and Kjell Erik Rian. Large-eddy simulation of the flow over a circular cylinder at Reynolds number 3900 using the OpenFOAM toolbox. *Flow, turbulence and combustion*, 89(4):491–518, 2012.

[54]Ali Mani, Parviz Moin, and Meng Wang. Computational study of optical distortions by separated shear layers and turbulent wakes. *Journal of Fluid Mechanics*, 625:273–298, 2009.

[55]Eric Garnier, Nikolaus Adams, and Pierre Sagaut. *Large Eddy simulation for compressible flows*. Springer Science & Business Media, 2009.

[56]M Pino Martin, Ugo Piomelli, and Graham V Candler. Subgrid-scale models for compressible large-eddy simulations. *Theoretical and Computational Fluid Dynamics*, 13(5):361–376, 2000.

[57]AW Vreman. An eddy-viscosity subgrid-scale model for turbulent shear flow: Algebraic theory and applications. *Physics of fluids*, 16(10):3670–3681, 2004.

[58]BA Kader and AM Yaglom. Heat and mass transfer laws for fully turbulent wall flows. *International Journal of Heat and Mass Transfer*, 15(12):2329–2351, 1972.

[59]Christoffer Norberg. An experimental investigation of the flow around a circular cylinder: influence of aspect ratio. *Journal of Fluid Mechanics*, 258:287–316, 1994.

[60]C Norberg and B Sunden. Turbulence and Reynolds number effects on the flow and fluid forces on a single cylinder in cross flow. *Journal of Fluids and Structures*, 1(3):337–357, 1987.

[61]X Ma, G-S Karamanos, and GE Karniadakis. Dynamics and low-dimensionality of a turbulent near wake. *Journal of Fluid Mechanics*, 410:29–65, 2000.

[62]J Franke and W Frank. Large Eddy simulation of the flow past a circular cylinder at ReD= 3900. *Journal of Wind Engineering and Industrial Aerodynamics*, 90(10):1191–1206, 2002.

[63]Arthur G Kravchenko and Parviz Moin. Numerical studies of flow over a circular cylinder at ReD= 3900. *Physics of Fluids*, 12(2):403–417, 2000.

[64]Joel H Ferziger, Milovan Perić, and Robert L Street. *Computational methods for fluid dynamics*, volume 3. Springer, 2002.